atmosphere

MDPI

Article

Monitoring Aerosol Dynamics in the Beijing–Tianjin–Hebei Region: A High-Resolution, All-Day AOD Dataset from 2018 to 2023

Jinyu Yang, Boqiong Zhang, Yiyao Yang, Sijia Liu, Bo Li, Wenhao Zhang * and Xiufeng Yang

School of Remote Sensing and Information Engineering, North China Institute of Aerospace Engineering, Langfang 065000, China; yjy19920111@stumail.nciae.edu.cn (J.Y.); zhang_boqiong@stumail.nciae.edu.cn (B.Z.); yangyiyao@stumail.nciae.edu.cn (Y.Y.); liusijia1007@stumail.nciae.edu.cn (S.L.); libo@stumail.nciae.edu.cn (B.L.); yangxf_hhyg@nciae.edu.cn (X.Y.)

* Correspondence: zhangwh@radi.ac.cn

Abstract

The Beijing–Tianjin–Hebei (BTH) region is a critical political and economic hub in China, which has long faced challenges related to atmospheric conditions. Traditional aerosol optical depth (AOD) monitoring methods suffer from issues of data discontinuity and gaps, limiting the ability for continuous long-term observation of aerosols. Aerosols have significant impacts on climate change and air quality, with AOD serving as a key indicator for characterizing atmospheric particulate concentration. Therefore, this study applied a machine learning model to improve all-day AOD estimation based on ground-level air quality and meteorological data, generating a long-term dataset spanning from 2018 to 2023. The results of the all-day AOD estimation method were evaluated through comparisons with Himawari-8, the Aerosol Robotic Network (AERONET), and the Copernicus Atmosphere Monitoring Service (CAMS). The estimated AOD demonstrated good agreement with AHI data, achieving an annual R^2 greater than 0.96 and RMSE less than 0.1. Spatially, the estimated AOD also showed strong consistency with AHI, AERONET, and CAMS. Additionally, the annual, seasonal, and hourly distribution characteristics of AOD from 2018 to 2023 were analyzed. Two typical cases of aerosol variation in the BTH region were selected and examined: a dust storm event in 2023 and changes during the Spring Festival in 2021. This method provides continuous data support for air pollution monitoring and control in the BTH region and offers valuable references for pollution prevention efforts.

Keywords: Beijing–Tianjin–Hebei; aerosol optical depth; machine learning; all-day

Check for updates

Academic Editors: Antonio Donateo, Marius M. Cazacu and Florin Unga

Received: 16 December 2025
Revised: 28 January 2026
Accepted: 30 January 2026
Published: 4 February 2026

Copyright: © 2026 by the authors. Licensee MDPI, Basel, Switzerland. This article is an open access article distributed under the terms and conditions of the Creative Commons Attribution (CC BY) license.

1. Introduction

Atmospheric aerosols consist of particles, either liquid or solid, that are dispersed in the air, generally varying in size from 10^{-3} μm to 10^{2} μm. Aerosols are classified into two main types: primary and secondary [1]. Primary aerosols are made up of particles that are released directly into the atmosphere from various sources. On the other hand, secondary aerosols arise from the chemical reactions of gaseous precursors such as sulfur dioxide (SO_2), nitrogen oxides (NO_x), and volatile organic compounds (VOCs) within the atmosphere. Atmospheric aerosols affect both weather and climate through their direct and indirect radiative forcing effects. These atmospheric components also significantly influence regional air quality and have implications for human health [2]. Aerosol optical depth (AOD) indicates the cumulative amount of the aerosol extinction coefficient, which

is measured from the Earth's surface through the upper atmospheric layers. It serves as an essential parameter for evaluating aerosol concentration [3]. Ground-based aerosol monitoring utilizes surface-based aerosol optical remote sensing instruments to observe solar radiation from the Earth's surface, thereby obtaining comprehensive aerosol layer information. For example, the Aerosol Robotic Network (AERONET) utilizes sun–sky–moon photometers to monitor the optical properties of aerosols across a vast array of stations over long periods [4]. AERONET data have an uncertainty of approximately ± 0.02, making them a commonly used benchmark for validating satellite data products [5]. The scarce and unevenly distributed monitoring stations, along with the sensitivity of instrumental measurements to specific meteorological factors like cloud cover and precipitation, frequently hinder the attainment of continuous spatiotemporal monitoring for ground-based AOD [6]. In contrast, satellite sensors can provide large-area, spatiotemporally continuous AOD observations [7,8]. At present, the satellite sensors that are frequently used consist of the Moderate Resolution Imaging Spectroradiometer (MODIS) aboard the polar-orbiting Terra and Aqua satellites, along with the Advanced Himawari Imager (AHI) featured on the geostationary satellite named Himawari-8. However, satellite monitoring often relies on radiative transfer models to quantitatively retrieve observed values of solar radiation received by remote sensors after undergoing coupled interactions with the atmosphere and Earth's surface. Consequently, these common satellite sensors can only operate during the daytime.

Atmospheric aerosols exhibit rapid spatiotemporal variations with pronounced diurnal differences [9]. The primary reasons are as follows: first, the stable atmospheric boundary layer and reduced turbulence activity at night limit pollutant dispersion, leading to elevated aerosol concentrations; second, many high-pollution production activities restricted during the day are shifted to nighttime operations. To establish a diurnal aerosol monitoring system, researchers have begun utilizing nighttime moonlight or ground-based artificial light for their studies [10–12].

AERONET deploys the new CE318-T photometer for observations [4]. The CE318-T is capable of detecting solar radiation during the day and the minimal energy that the moon reflects at night, thus offering insights into water vapor and aerosols present at night. Zhou et al. [13] employed a lunar-based backscattering algorithm grounded in the unified linear vector radiative transfer model to retrieve nocturnal AOD over rural areas in the United States. However, due to the limited radiative energy of moonlight—merely 1/40 millionth of solar irradiance—the CE318 instrument can only perform aerosol monitoring when lunar illumination exceeds 50%, which even under ideal observational conditions allows coverage of merely 50% of monthly nocturnal periods [5,14]. Furthermore, moonlight-based inversion methods are susceptible to interference from terrestrial light sources, thereby imposing significant temporal and spatial constraints on this approach. With the launch of satellites equipped with low-light detection capabilities, researchers have begun exploring satellite-based methodologies for nocturnal AOD retrieval using weak light signals [15]. Zhang conducted qualitative analyses of nocturnal surface light attenuation [16], utilizing visible and near-infrared channel data from the Defense Meteorological Satellite Program's Operational Linescan System (DMSP/OLS), demonstrating the feasibility of satellite-derived nocturnal AOD inversion. Nevertheless, this technique remains constrained by inherent limitations in nighttime aerosol identification and quantitative inversion stemming from radiometric similarities between nocturnal aerosols and clouds, as well as restricted observational capabilities. A method was proposed by Johnson et al. [17] to obtain AOD by leveraging the variation between the radiation from ground light sources and the dark background radiation detected by the VIIRS/DNB. McHardy et al. [18] developed a method using spatial variance in urban light emissions from VIIRS/DNB data to retrieve nocturnal

AOD. Building on McHardy's approach, Zhang et al. [19] maintained the term of surface diffuse reflection and employed the spatial standard deviation of artificial lighting sources to reverse-engineer nighttime AOD. Wang et al. [20] conducted a study in four representative cities in China to examine the relationship between nighttime light radiance as measured by VIIRS/DNB and AOD in various urban settings. They observed variations in the correlation between nighttime light radiance and AOD, influenced by differing levels of urbanization and climatic conditions. Jiang et al. [21] applied data from VIIRS/DNB to obtain nighttime AOD in North China, using the principles of atmospheric radiative transfer theory. Li et al. [22] demonstrated the feasibility of retrieving AOD using a radiatively stable integrating sphere and a satellite-based low-light channel. Meng et al. [23] reversed the nighttime AOD by taking into account both natural and artificial sources of illumination simultaneously. However, the diminished radiation energy that satellite sensors receive during nighttime complicates the task of differentiating the subtle aerosol signal from the land surface. Furthermore, due to the uncertainty of urban light radiation and its significant temporal variation trends, ground-based light inversion algorithms introduce additional uncertainty. Consequently, the establishment of continuous day-and-night aerosol monitoring has emerged as an issue that requires immediate resolution.

The northwest high and southeast low topography in the BTH region is unfavorable for pollutant dispersion. Severe air pollution caused by dense population, concentrated industrial activities, substantial energy consumption, and significant vehicle emissions has become a major threat to ecosystems and human health. However, atmospheric aerosol monitoring faces limitations due to spatial and temporal resolution constraints of ground-based observations and satellite remote sensing, particularly under nighttime conditions and adverse weather scenarios. Despite being one of China's most important economic, cultural, and political centers, the study area contains only four AERONET sites capable of providing nocturnal AOD data, which are insufficient to comprehensively characterize regional nighttime aerosol properties. Accurate monitoring and validation of long-term aerosol trends are crucial for understanding regional aerosol sources, as these particles exert significant impacts on climate change, air quality, and human health [2]. Therefore, to better understand and quantify atmospheric aerosols in the BTH region and investigate their spatiotemporal distribution characteristics and trends, it is imperative to conduct AOD monitoring studies based on all-day, long-term time series. In this study, we integrated ground-based air quality monitoring data with multi-level meteorological data to construct an all-day AOD estimation model, generating a high spatiotemporal resolution all-day AOD dataset covering the BTH region from 2018 to 2023. This dataset features a temporal resolution of 1 h and a spatial resolution of 0.05°, providing crucial data support for detailed studies of aerosol spatiotemporal distribution within the region. Additionally, this paper explores the practical application of this all-day AOD monitoring technology in special events such as severe pollution episodes and major events. This study not only provides data support for monitoring and controlling air pollution in the BTH region but also offers insights for climate change research and the formulation of air pollution control strategies in similar areas.

2. Data and Methods

2.1. Data

2.1.1. Surface Air Quality Data

Ground-based air quality data were obtained from the China National Environmental Monitoring Center. Ground-level air quality monitoring stations typically employ beta-ray attenuation or tapered element oscillating microbalance methods to measure particulate matter concentrations [24,25]. These measurements exhibit an uncertainty below 0.75%,

with hourly average accuracy reaching ±1.5 μg/m^3 [26]. The dataset includes measured values of AQI, $PM_{2.5}$, PM_{10}, SO_2, NO_2, O_3, and CO from a total of 135 air quality monitoring stations [24], whose spatial distribution is illustrated in Figure 1.

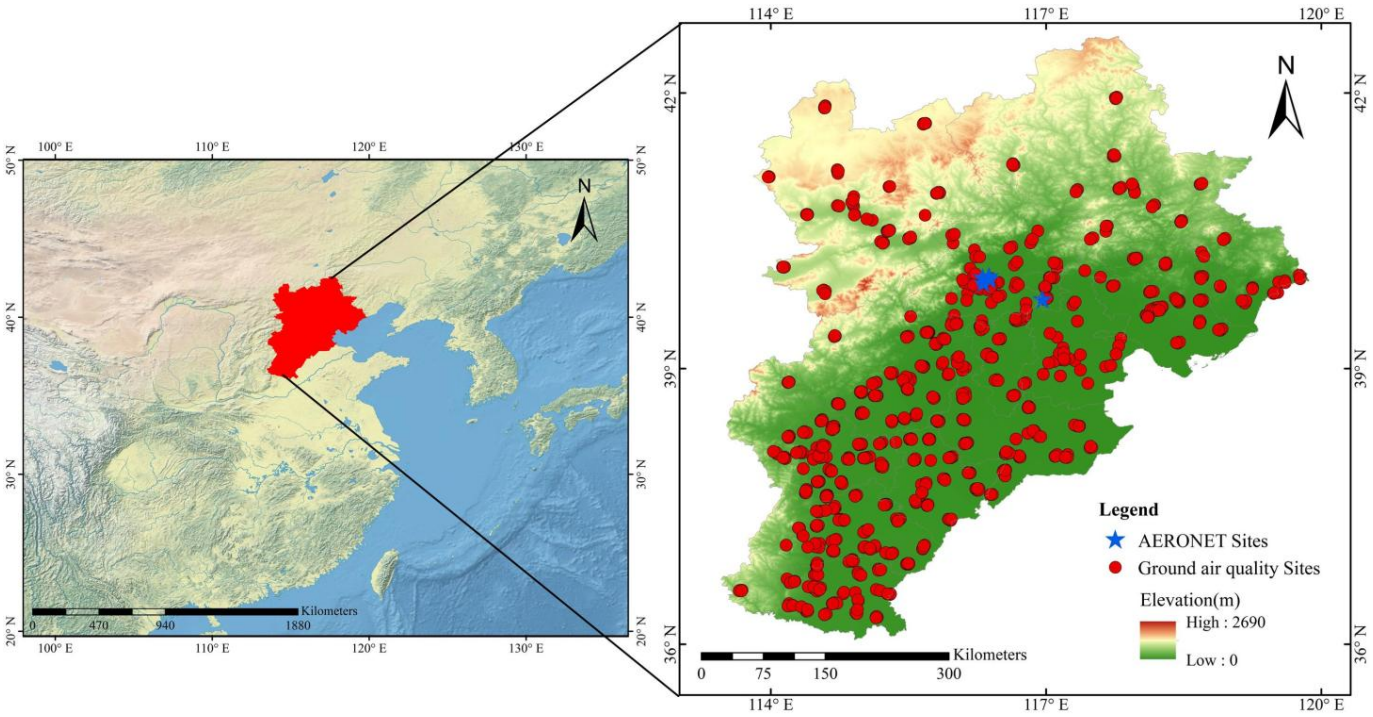


Figure 1. Spatial distribution of ground air quality monitoring stations and AERONET stations in BTH.

2.1.2. Meteorological Data

The meteorological data information was sourced from the ERA5 reanalysis dataset, which is offered by the European Centre for Medium-Range Weather Forecasts (ECMWF). The dataset encompasses hourly data presented in both single-level and pressure-level formats from 1940 up to the present day, offering a temporal resolution of one hour along with a spatial resolution of 0.25° [27]. This study utilized hourly ERA5 data from 2018 to 2023, including the 10 m u-component of wind (U10), 10 m v-component of wind (V10), surface pressure (SP), boundary layer height (BLH), 2 m temperature (T2M), relative humidity (RH), temperature (T), u-component of wind (U), and v-component of wind (V) at pressure levels of 1000 hPa, 850 hPa, 700 hPa, 500 hPa, 400 hPa, 300 hPa, and 200 hPa.

2.1.3. AOD Products

The dataset consists of AHI AOD information obtained from the Japan Aerospace Exploration Agency (JAXA), incorporating L3-level aerosol measurements at a wavelength of 500 nm. These retrievals demonstrate a temporal resolution of one hour and a spatial resolution of 0.05° [6].

The AERONET is a global network providing high-accuracy ground-based aerosol data; its observation of AOD is based on sun–sky–moon photometers [28]. In this study, it was used to validate the estimated all-day AOD. The following AERONET stations were selected: Beijing, Beijing-CAMS, Beijing_PKU, and Xianghe.

The global AOD reanalysis dataset is supplied by the Copernicus Atmosphere Monitoring Service (CAMS) [29]. This study employed CAMS AOD data at a wavelength of 500 nm to validate the predicted all-day AOD, which has a temporal resolution of one hour and a spatial resolution of 0.4°.

2.1.4. Geographic Data

The Version 6 MODIS Normalized Difference Vegetation Index (NDVI) product offers a temporal resolution of 16 days and a spatial resolution of 0.05 degrees. It is a Climate Modeling Grid (CMG) dataset generated from the original 1 km resolution NDVI product (MYD13A2) [30].

The Shuttle Radar Topography Mission (SRTM) was a collaborative initiative that effectively gathered elevation information for more than 80% of the planet's terrestrial area, spanning from 60° N to 56° S [31]. The SRTM1 product (1 arc-second resolution) provides elevation data with an absolute vertical accuracy of approximately 30 m.

2.2. Methods

2.2.1. All-Day AOD Estimation Workflow

Figure 2 depicts the workflow for the estimation of all-day AOD implemented in this study. The procedure encompasses four components: data collection and preprocessing, construction of a sample dataset, development and validation of an all-day AOD model, and Kriging interpolation for generating long-term time series datasets.

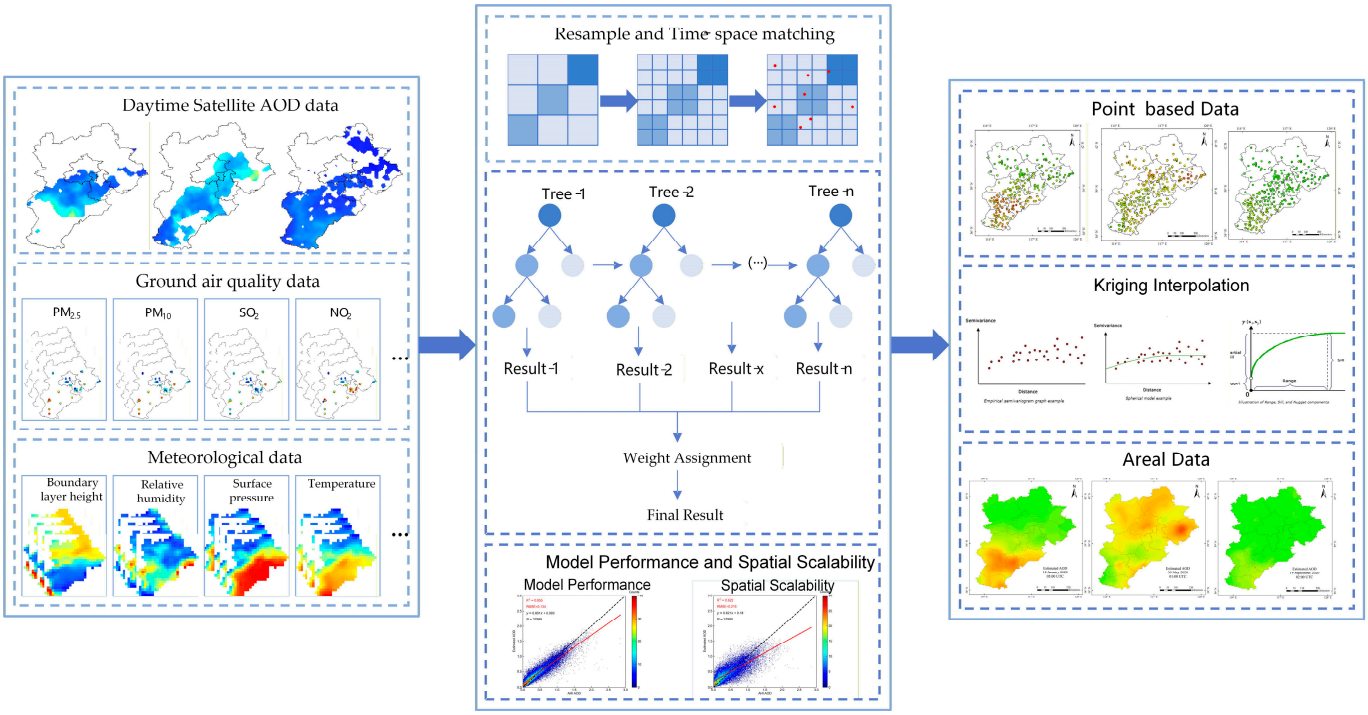


Figure 2. All-day AOD estimation workflow.

2.2.2. Data Preprocessing

The dataset comprised satellite aerosol data, meteorological data, ground-based air quality monitoring data, and elevation data. The data were first spatiotemporally matched; time was standardized to Coordinated Universal Time (UTC), and spatial resolution was resampled to 0.05°. Then, valid data were extracted and merged with strict quality control measures to ensure reliability and the high quality of the dataset. Considering the potential presence of outliers in the data from provincial air quality monitoring stations, a reasonable range should be established for the original observational data to exclude missing values and outliers. Finally, we obtained a dataset that had been aggregated from the ground air quality monitoring information, meteorological data, and satellite aerosol measurements (Table 1).

Table 1. Descriptive statistics of datasets.

Category		Variable	Content	Units	Spatial Solution	Temporal Resolution
Ground data		$PM_{2.5}$	1 h average	$\mu g/m^3$	site	Hourly
		PM_{10}	1 h average	$\mu g/m^3$	site	Hourly
		SO_2	Average sulfur dioxide in one hour	$\mu g/m^3$	site	Hourly
		NO_2	Average nitrogen dioxide in one hour	$\mu g/m^3$	site	Hourly
		O_3	One-hour average of ozone	$\mu g/m^3$	site	Hourly
		CO	Average of carbon monoxide	$\mu g/m^3$	site	Hourly
Meteorological data	Single-level	BLH	Boundary layer height	m	0.25°	Hourly
		SP	Surface pressure	Pa	0.25°	Hourly
		T2M	2 m temperature	K	0.25°	Hourly
		U10	10 m u-component of wind	m/s	0.25°	Hourly
		V10	10 m v-component of wind	m/s	0.25°	Hourly
	Multi-level	RH	Relative humidity	%	0.25°	Hourly
		T	Temperature	K	0.25°	Hourly
		U	u-component of wind	m/s	0.25°	Hourly
		V	v-component of wind	m/s	0.25°	Hourly
Geographical data		NDVI	Normalized difference segmentation index	-	0.05°	16 days
		DEM	Digital elevation model	m	-	-
Satellite data		AOD	Aerosol optical depth	-	0.05°	Hourly

2.2.3. Construction of All-Day AOD Estimation Model

The all-day AOD estimation model is based on the XGBoost. The XGBoost regression model is used for the prediction of continuous numerical target variables [32]. The model operates within the gradient boosting decision tree (GBDT) framework, achieving predictions by iteratively building multiple decision trees and optimizing the prediction error at each step (Figure 3). In this study, the Bayesian optimization method was employed to automatically tune the key hyperparameters of XGBoost, thereby determining the optimal parameter combination (Table A2) and constructing the final all-daytime AOD estimation model.

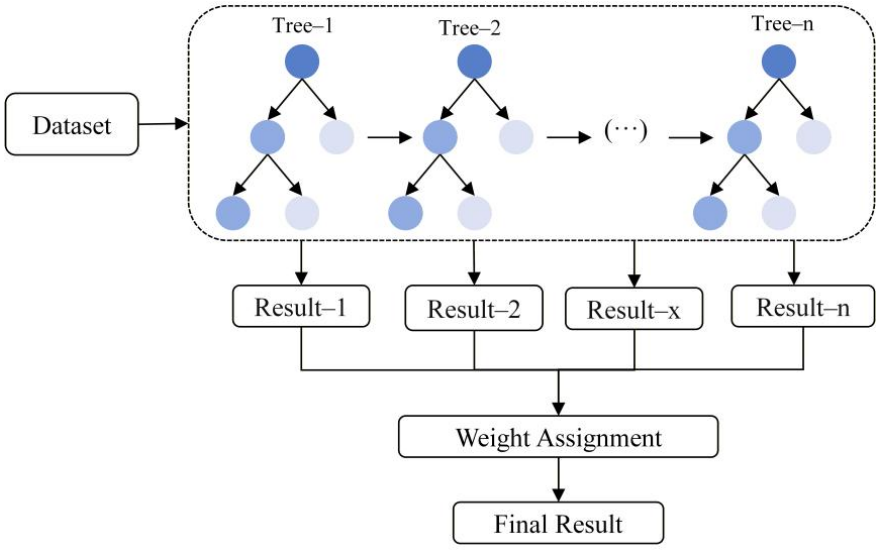


Figure 3. The XGBoost model.

2.2.4. Kriging Interpolation

Kriging interpolation is a geostatistical method that estimates values at unknown locations using data from known points. Its core principle relies on spatial correlation, where the value at each point is influenced not only by distance but also by the overall spatial arrangement of the data points. Kriging interpolation uses a variogram to model spatial dependence and provides optimal estimates for unknown points by minimizing estimation error [33].

2.2.5. Model Evaluation

The model was evaluated using ten-fold cross-validation and leave-one-city-out cross-validation (Figure 4) [30,34].

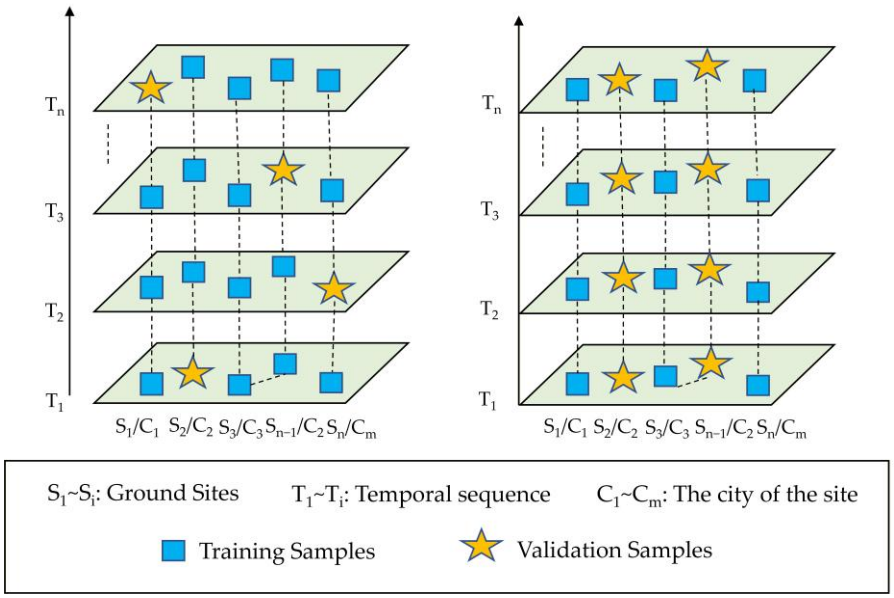


Figure 4. The ten-fold cross-validation method and leave-one-city-out cross-validation method based on sample data. (The arrows indicate the chronological order of the time series, while the dashed lines represent the correspondence between the same sample at different time steps).

1. The ten-fold cross-validation method based on sample data involved dividing the dataset into 10 subsets, using 9 of these subsets as training data, while the remaining subset was utilized for validation. This process was repeated 10 times to evaluate the trained model with the test dataset.
2. The leave-one-city-out cross-validation approach consisted of partitioning the dataset based on "city". In this research, there were 13 cities, resulting in 13 distinct subsets. The data from 12 of these cities served as training data, while the data from the one remaining city was utilized for validation. This procedure was performed 13 times to assess the performance of the trained model using the test dataset.

The results of the verification process are expressed in terms of two statistical metrics: the coefficient of determination, commonly denoted as R^2, and the root mean square error, abbreviated as RMSE. These metrics serve as essential indicators of the accuracy and reliability of the model being assessed. The methodologies for computing the coefficient of determination and the root mean square error are detailed in Equations (1) and (2), respectively, which outline the necessary calculations to derive these values.

$$R^2 = 1 - \frac{\sum_{i=1}^{n}\left(AOD_{Ture,i} - AOD_{Estimated,i}\right)^2}{\sum_{i=1}^{n}\left(AOD_{Ture,i} - AOD_{Average,i}\right)^2} \quad (1)$$

$$\mathrm{RMSE} = \sqrt{\frac{1}{n}\sum_{i=1}^{n}\left(AOD_{Ture,i} - AOD_{Estimated,i}\right)^2} \quad (2)$$

3. Results

3.1. Model Performance

3.1.1. Sample-Based Cross-Validation

Figure 5 presents the all-day AOD estimation results for the BTH region from 2018 to 2023, validated using ten-fold cross-validation. The AHI AOD is depicted on the X-axis, while the estimated AOD is shown on the Y-axis. The annual sample size exceeds 200,000. The sample sizes used for each year were as follows: 145,152 in 2018, 363,399 in 2019, 326,550 in 2020, 212,653 in 2021, 307,918 in 2022, and 325,353 in 2023.

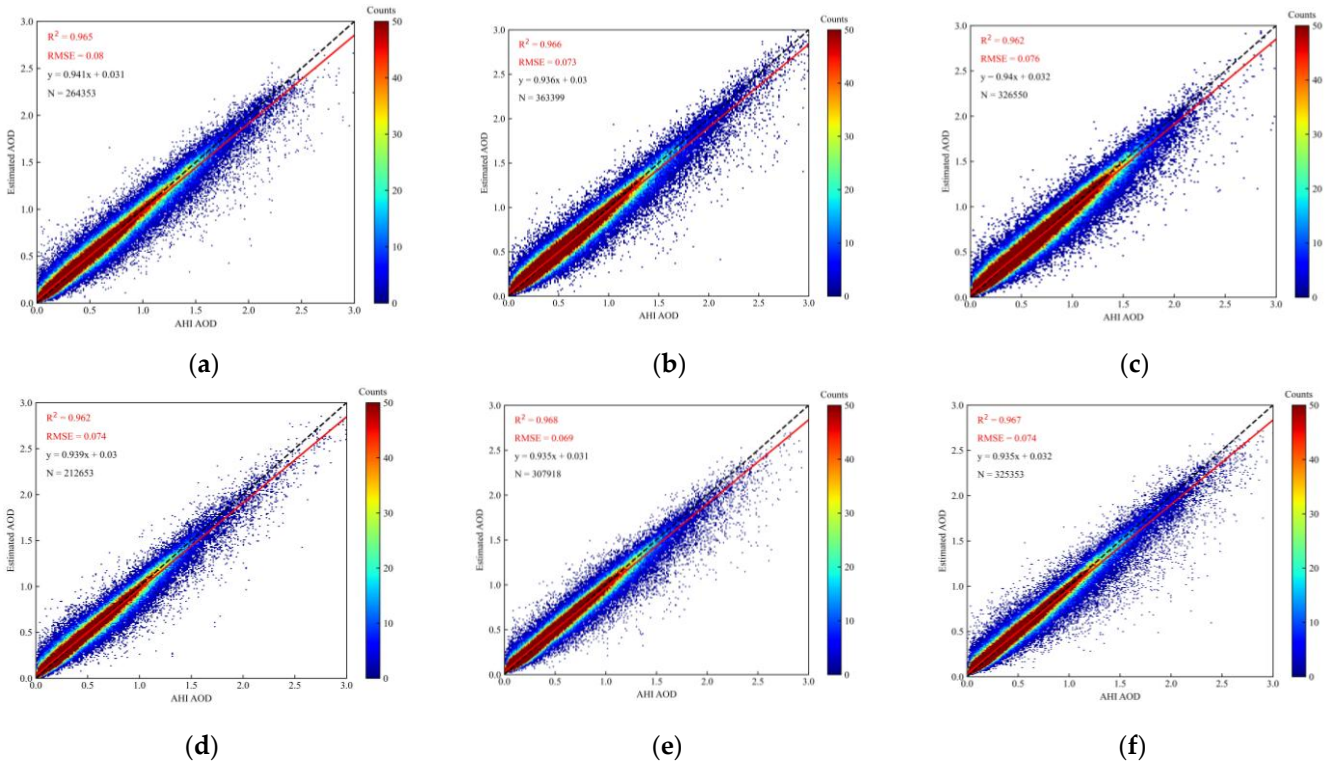


Figure 5. The results of all-day AOD estimation models in the BTH region from 2018 to 2023 based on sample cross-validation. (**a**) 2018; (**b**) 2019; (**c**) 2020; (**d**) 2021; (**e**) 2022; (**f**) 2023. (The dashed line represents the fitted curve, and the red line indicates the 1:1 reference line).

The R^2 values for each annual model surpassed 0.96, varying between 0.962 and 0.968, with an average of 0.965, thus indicating exceptional predictive accuracy. The RMSE values were all less than 0.1; to be precise, they ranged from 0.069 to 0.08, with a mean of 0.074, denoting minimal estimation error. The high R^2 values in conjunction with the low RMSE suggest that the model upholds outstanding accuracy and robustness across different years. Furthermore, the slope of each annual model was less than 1, fluctuating between 0.935 and 0.941, implying that the models tend to slightly underestimate. However, the overall performance of the models remained commendable, with low error levels and dependable AOD estimates. Moreover, the model's consistent performance over a six-year period attests to its reliability and temporal consistency in estimating AOD.

3.1.2. Cross-Validation Based on Leave-One-City-Out

Figure 6 illustrates the results of all-day AOD estimation in the BTH region from 2018 to 2023, as validated by the leave-one-city-out cross-validation method. The R^2 values for each annual model were consistently above 0.8, varying between 0.817 and 0.847, with an average of 0.833. All RMSE values were below 0.2, ranging from 0.16 to 0.175, with an average of 0.162. The slope of each annual model remained consistently below 1, ranging from 0.79 to 0.81. These results indicate that the all-day AOD estimation models exhibit robust spatial scalability in the context of leave-one-city-out cross-validation.

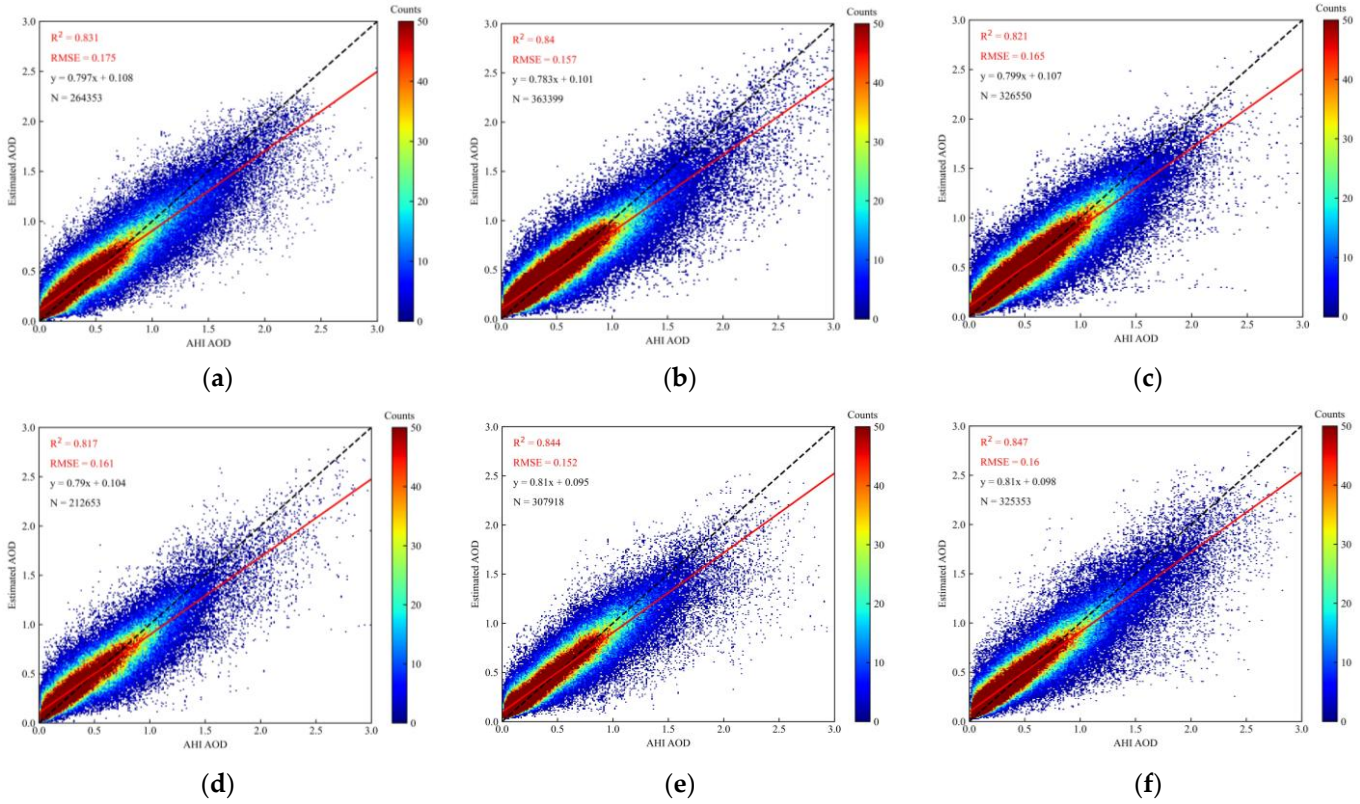


Figure 6. The all-day AOD estimation models in the BTH region from 2018 to 2023 based on the leave-one-city-out cross-validation. (**a**) 2018; (**b**) 2019; (**c**) 2020; (**d**) 2021; (**e**) 2022; (**f**) 2023. (The dashed line represents the fitted curve, and the red line indicates the 1:1 reference line).

The heatmaps presented in Figure 7 illustrate the R^2 and RMSE values for each city within the BTH region, with the years indicated on the X-axis and the cities on the Y-axis. As shown in Figure 7, Hengshui and Langfang had the best performance, with R^2 ranging from 0.876 to 0.916 and 0.876 to 0.910, respectively, and with RMSE ranging from 0.12 to 0.146 and 0.12 to 0.136, respectively. Zhangjiakou has the worst performance, with R^2 and RMSE ranging from 0.461 to 0.598 and 0.149 to 0.19, respectively. The terrain of the BTH region is complex, and the industrial differentiation is large. There are heavy industrial cities, such as Hengshui and Langfang, and ecological tourism cities, such as Zhangjiakou. From 2018 to 2023, the average annual $PM_{2.5}$ concentration in Hengshui City was 49.83 μg/m^3, and the lowest and highest annual averages were 42 μg/m^3 in 2021 and 62 μg/m^3 in 2018, respectively. The average annual $PM_{2.5}$ concentration in Zhangjiakou City was 22.5 μg/m^3, and the lowest and highest annual averages were 17 μg/m^3 in 2022 and 29 μg/m^3 in 2018, respectively. Table A1 shows the annual average $PM_{2.5}$ concentration estimated for each city in the BTH region. The heavy industrial cities have higher R^2 and lower RMSE, while ecological cities have lower R^2 and higher RMSE. The difference in model performance may be attributed to the fact that heavy industrial cities are dominant in the BTH region, where

the model is mainly trained and performs well in representing atmospheric conditions. When applied to cities with different industrial structures and atmospheric conditions, the model has a small degradation, which may also reflect the influence of local aerosol properties and atmospheric circulations. Overall, the all-day AOD estimation model can still give reasonable and valuable estimates across different urban backgrounds.

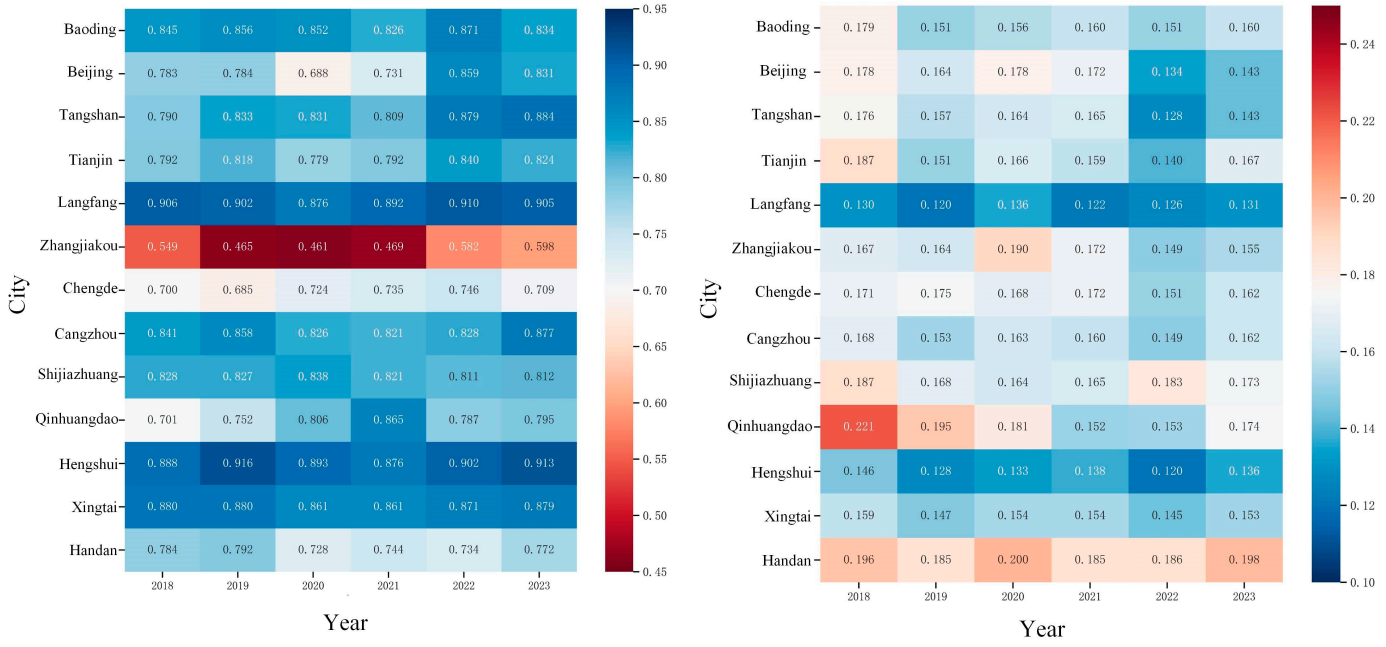


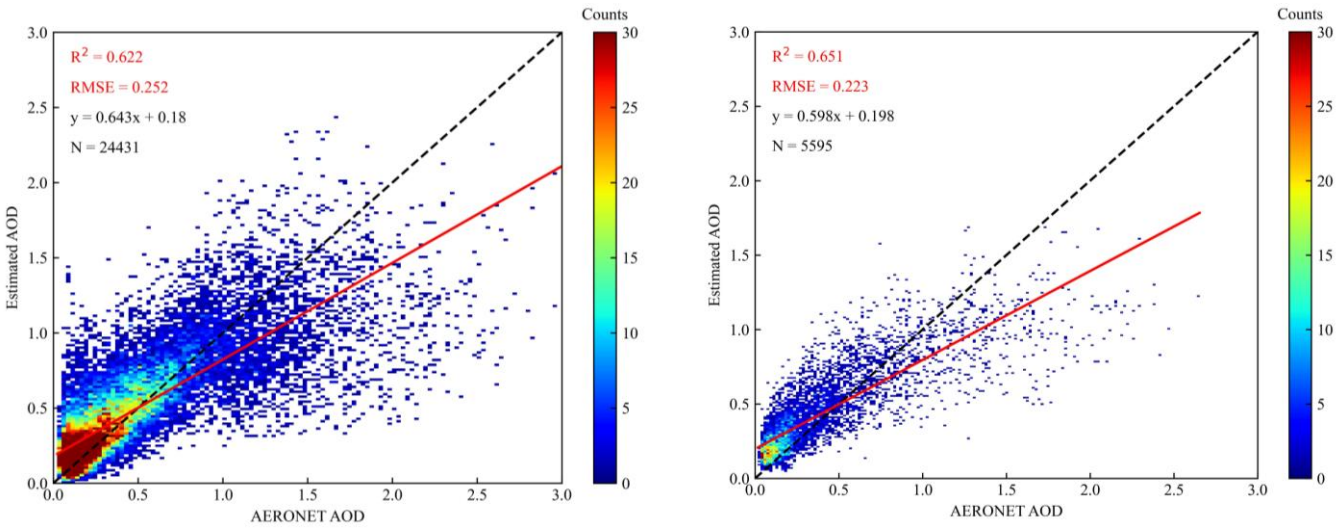
Figure 7. Heat maps of R2 and RMSE of cities. (**a**) R2 for each city (leave-one-city-out cross-validation). (**b**) RMSE for each city (leave-one-city-out cross-validation).

3.2. Comparison with AOD Products

3.2.1. Model Accuracy Assessment

To enhance the validation of the all-day AOD estimation model's accuracy, AOD at 500 nm from four AERONET stations within the research domain between 2018 and 2023 was employed. Recognizing the AERONET data's temporal resolution as 3 min, a 5 min time window, centered on each complete hour, was chosen. The mean value within this window was computed and compared to the model's estimated value, allowing for the exclusion of invalid data points.

Figure 8 shows the scatter plots of model-estimated AOD from the all-day retrieval algorithm versus AERONET AOD measurements. Figure 8a presents the daytime estimated AOD vs. AERONET AOD, using a total of 24,431 matched data in the daytime comparison. The results show good agreement between estimated values and observations with an R^2 of 0.622, RMSE of 0.252, and slope of 0.643. Figure 8b shows the nighttime estimated AOD vs. AERONET AOD using a total of 5595 matched data for nighttime comparison. The results show good agreement between estimated values and observations with an R^2 of 0.651, an RMSE of 0.223, and a slope of 0.598.



(**a**) (**b**)

Figure 8. The fitting scatter plot of the estimates of AOD and AERONET. (**a**) Daytime; (**b**) Nighttime. (The dashed line represents the fitted curve, and the red line indicates the 1:1 reference line).

Figure 9 shows the error histogram and diurnal variation in errors between the estimated (or AHI) AOD and AERONET AOD. In Figure 9a,c,e, the horizontal axes represent the error between estimated AOD or AHI AOD and AERONET AOD (X-AERONET), and the vertical axes represent the frequency of errors within each bin interval. Figure 9a gives the error histogram between the four AERONET stations' AOD measurements in the BTH region at daytime and their corresponding estimated AOD values and AHI AOD data. As shown in Figure 9a, the red solid line represents the fitted normal distribution curve of the average error between daytime AOD estimates and AERONET AOD, while the blue dashed line represents the fitted normal distribution curve of the average error between AHI AOD and AERONET AOD. The mean error of estimated AOD at daytime to AERONET was 0.0483 with a standard deviation (Std) of 0.2118, indicating an overestimation of the AOD relative to AERONET with a wide and dispersed error distribution. The average discrepancy between AHI AOD and AERONET AOD was 0.0806, accompanied by a standard deviation of 0.2035. Although the average error of AHI AOD is greater, the marginally lower standard deviation indicates that the distribution of errors is more tightly clustered. The smaller mean error of the estimated AOD shows it is closer to AERONET AOD than AHI AOD.

Figure 9c,e display the error histograms for estimated AOD compared to AERONET AOD during daytime and nighttime at the Beijing-CAMS and Beijing_PKU stations, respectively. The red solid line represents the fitted normal distribution curve of the mean error between daytime AOD estimates and AERONET AOD, while the blue dashed line represents the fitted normal distribution curve of the mean error between nighttime AOD estimates and AERONET AOD. At the Beijing-CAMS station, the average discrepancy between the estimated daytime AOD and the AERONET AOD was 0.0549, accompanied by a standard deviation of 0.2017. For nighttime AOD estimated, the average error was 0.0703, with a standard deviation of 0.1868. These results imply that while the average error in nighttime AOD estimated is slightly higher than that of daytime estimated, the smaller standard deviation suggests a more concentrated distribution of errors during nighttime. At the Beijing_PKU station, the mean difference between daytime estimated AOD and AERONET AOD was 0.0359, with a standard deviation of 0.1933. For nighttime estimated AOD, the mean error was 0.0495, and the standard deviation was 0.1954. This indicates that the errors in nighttime AOD estimated are similar to those during daytime, although

both the mean error and standard deviation are slightly higher at night. Overall, at both the Beijing-CAMS and Beijing_PKU stations, the mean error between the estimated AOD and AERONET AOD remains low during both daytime and nighttime, demonstrating the high accuracy and temporal consistency of the model. Furthermore, minor variations in error characteristics across stations may be attributed to differences in local environmental conditions, topography, and meteorological factors.

Figure 9b,d,f show the time series of the difference between the daily estimated AOD and AERONET AOD from 2018 to 2023. Figure 9 reveals that the errors are mainly distributed in the range of -1 to 1. Although the daily estimated AOD has small errors compared with the AERONET AOD on the whole, they fluctuate greatly during a specific period. As shown in Figure 9, the discrepancies between estimated AOD and AERONET AOD exhibit certain seasonal periodic patterns both during daytime and nighttime. The estimated AOD is significantly overestimated during the daytime in 2020, 2021, 2022, and November to December 2023, which may be related to winter meteorological conditions, regional pollution events, or satellite observation errors. For example, stable winter meteorological conditions and high anthropogenic emissions can lead to high aerosol concentrations. In addition, low solar elevation angles (e.g., in winter) or complex weather conditions can reduce the accuracy of remote sensing inversion, thus increasing the estimation error. On the other hand, despite the relatively limited data volume of nighttime AERONET AOD measurements, the errors in estimated nighttime AOD values also exhibit periodic patterns similar to those observed in daytime AOD.

3.2.2. Time Comparison

To examine the diurnal variation in AOD, we selected four AERONET stations for analysis: Beijing, Beijing-CAMS, Beijing_PKU, and Xianghe. We compared the diurnal variations in AERONET AOD, estimated AOD, AHI AOD, and CAMS AOD, evaluating each, respectively. Both the Beijing-CAMS and Beijing_PKU stations provide daytime and nighttime AOD data, whereas the Beijing and Xianghe stations only offer daytime data. Figure 10 depicts the diurnal variation in AOD on specific days across these stations. The illustration indicates that the estimated AOD closely follows the diurnal variation patterns observed in AHI, CAMS, and AERONET AOD at all locations. Shaded areas in the figure represent nighttime periods. At the Beijing and Xianghe sites, the estimated AOD trends closely match the overall diurnal patterns observed in AHI and AERONET AOD. Furthermore, at the Beijing-CAMS and Beijing_PKU stations, which provide nighttime data, the estimated AOD trends show a high level of consistency with the AERONET AOD measurements taken during nighttime. This further underscores the high reliability of the estimation model under nocturnal conditions.

Figure 11 illustrates the monthly average fluctuations of four parameters: AERONET AOD, estimated AOD, AHI AOD, and CAMS AOD, across four AERONET sites, namely Beijing, Beijing-CAMS, Beijing_PKU, and Xianghe. The depiction in the figure suggests that the monthly variations in these four parameters largely align. The estimated AOD effectively encapsulates the spatiotemporal patterns of AOD, demonstrating substantial coherence with trends observed in other AOD products.

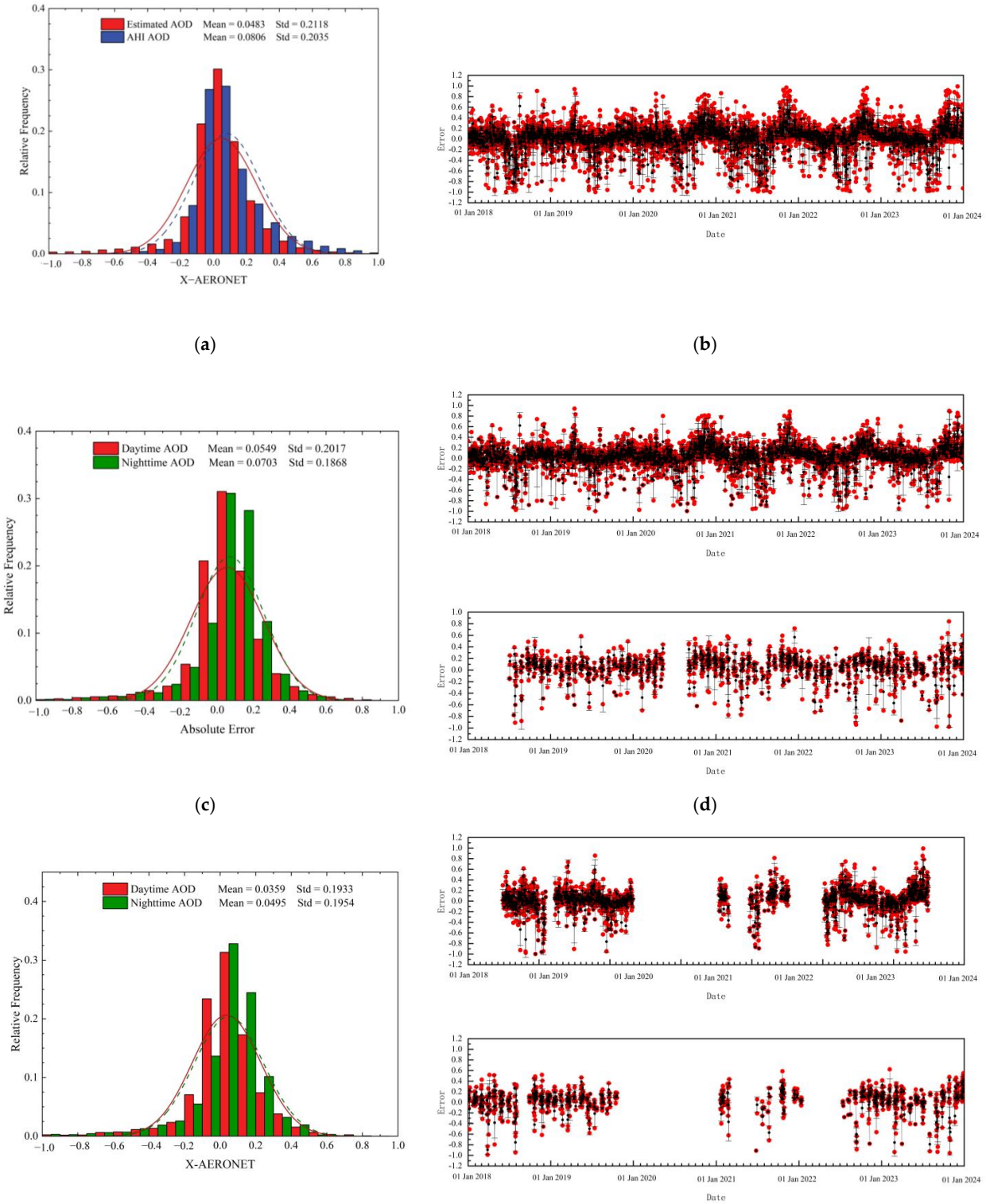
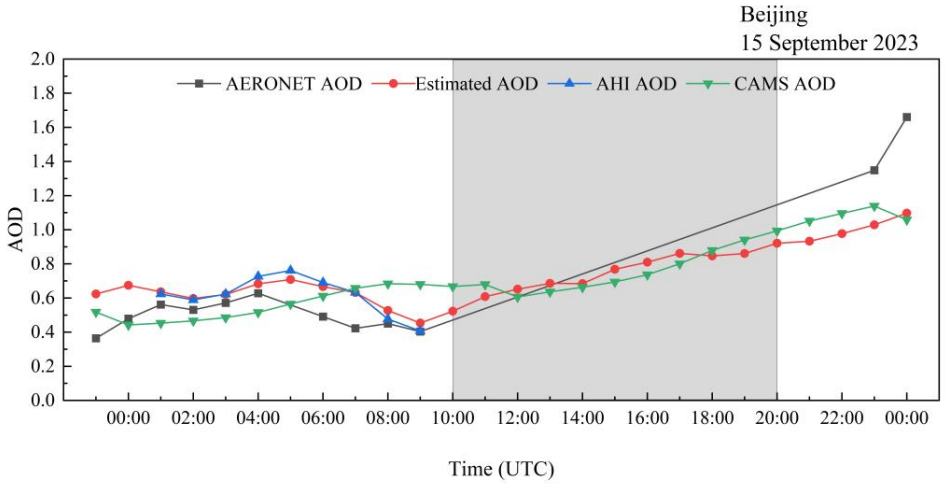


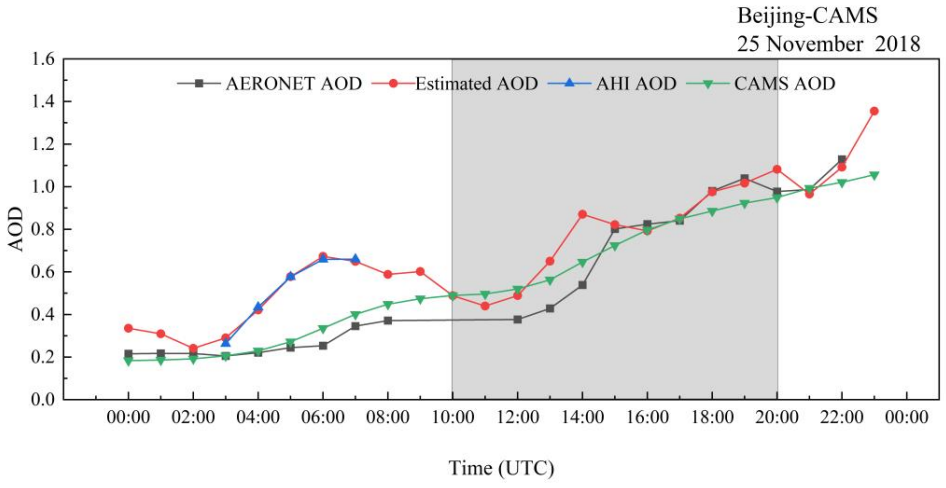
Figure 9. Error histogram and diurnal variation chart between the estimated value, AHI AOD, and AERONET AOD. (**a**) Histogram of estimated AOD, AHI AOD, and AERONET AOD error distribution. (**b**) Error bar plot of Daily estimated AOD versus AERONET AOD error from 2018 to 2023. (**c**) Histogram of estimated AOD and Beijing-CAMS site AOD error distribution. (**d**) Error bar plot of Daily estimated AOD versus Beijing-CAMS site AERONET AOD error from 2018 to 2023 (top panel: daytime; bottom panel: nighttime). (**e**) Histogram of estimated AOD and Beijing_PKU site AOD error distribution. (**f**) Error bar plot of Daily estimated AOD versus Beijing_PKU site AERONET AOD error from 2018 to 2023 (top panel: daytime, bottom panel: nighttime).

3.2.3. Spatial Comparison

To further compare and analyze the spatial distribution of AOD, the periods after winter snowfall, summer cloudy days, and autumn clear days were selected. Figure 12 illustrates the spatial distribution and variation in AHI AOD alongside the estimated AOD. Figure 12a–c show the spatial distributions of AHI AOD from satellite products at 05:00 UTC on 12 January 2020, 01:00 UTC on 30 May 2020, and 02:00 UTC on 19 September 2020, respectively. Figure 12d–f show the corresponding distributions of estimated AOD. Figure 12g–i show the absolute differences between the estimated AOD and AHI AOD. The overall spatial distribution of the estimated AOD appears to align well with that of AHI AOD, as demonstrated in the figure, with only minor discrepancies noted in several regions. Nevertheless, notable discrepancies are clearly evident between the projected AOD and the AHI AOD in the southern region of BTH under winter conditions following snowfall (Figure 12g). This is mainly due to the limited ability of satellite products to retrieve data in snow-covered areas. The presence of snow cover changes the surface reflectance characteristics, which affects the detection of aerosol signals from satellites.

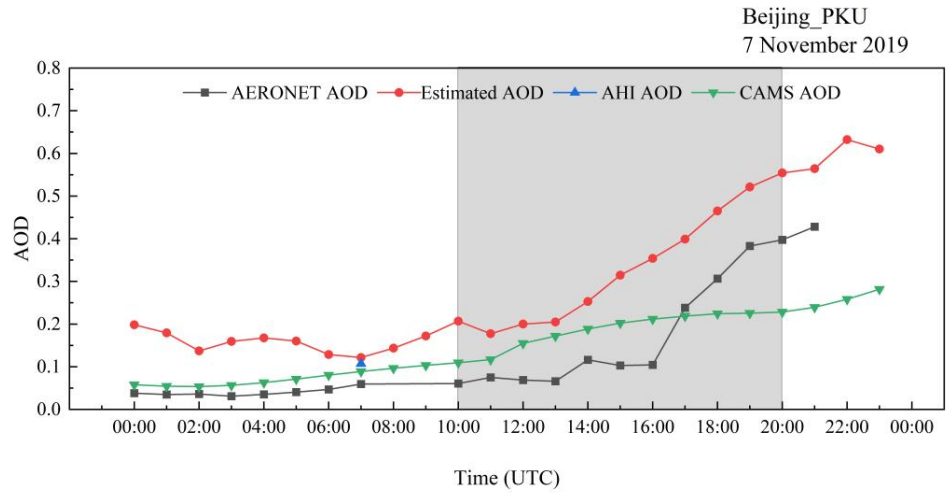


(**a**)

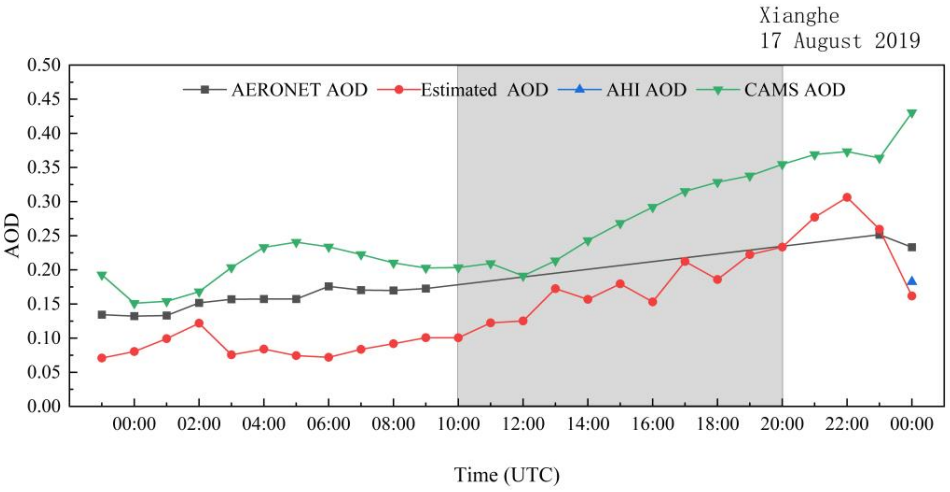


(**b**)

Figure 10. *Cont.*



(**c**)



(**d**)

Figure 10. Comparison of daily variation in AERONET AOD, estimated AOD, AHI AOD, and CAMS AOD at four AERONET stations. (**a**) Beijing (15 September 2023), (**b**) Beijing-CAMS (25 November 2018), (**c**) Beijing_PKU (7 November 2019), (**d**) Xianghe (17 August 2019). (Gray Area: The range of nighttime hours in the study area).

3.3. Temporal and Spatial Distribution of AOD in the Whole Day

3.3.1. Circadian Cycle

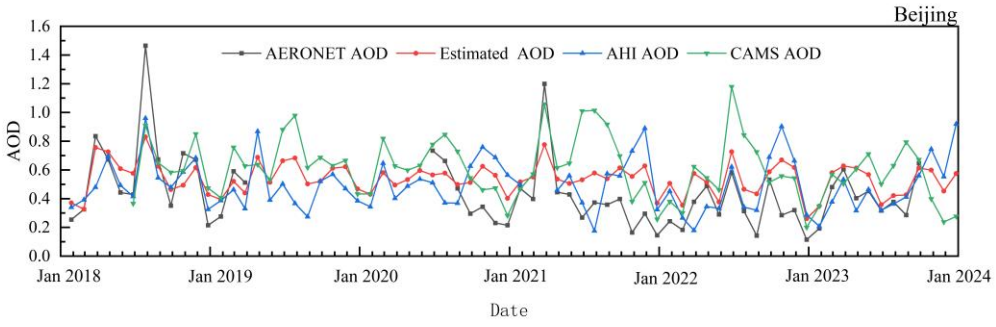
Figure 13 depicts the hourly average trend of AOD across cities in the BTH from 2018 to 2023, while Figure 14 shows the geographical distribution of this average during the same period. The data suggests that the hourly average AOD values for each city over these six years range between 0.3 and 0.7. Elevated AOD values are indicative of higher aerosol concentrations in the atmosphere, potentially linked to local pollution sources, meteorological conditions, and other environmental factors. With the exception of Zhangjiakou and Chengde, similar trends in hourly average AOD are observed across other cities. An initial decrease in the hourly average AOD is noted from 08:00 local time (00:00 UTC), which is then followed by an increase and subsequent decrease. A trough is observed around 11:00 local time (03:00 UTC) and a peak near 13:00 local time (05:00 UTC). This pattern implies the impact of diurnal fluctuations in human activities

and meteorological conditions on aerosol concentrations. The trend may be attributed to the cumulative effects of pollutant emissions and atmospheric dynamics. Although pollutants from human activities, such as nitrogen oxides and volatile organic compounds, gradually rise post 8 a.m., these substances necessitate time for chemical reactions to form secondary aerosols. As solar radiation intensifies, surface heating augments, bolstering atmospheric convection. This convective process carries surface pollutants to higher altitudes, accelerating photochemical reactions involving pollutants like NOx and VOCs when exposed to sunlight, leading to increased production of secondary aerosols. In the afternoon, atmospheric mixing stabilizes, facilitating the gradual diffusion of pollutants into the higher atmospheric layers.

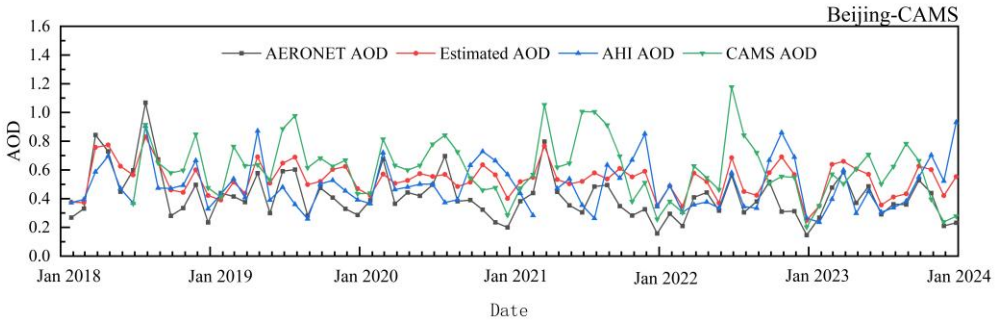
Hourly mean values of AOD exhibit variations across different cities, primarily influenced by the type and intensity of pollution sources, topographic and meteorological conditions, patterns of anthropogenic activities, the natural environment, and regional transport effects. Contributing factors include industrial and traffic emissions, meteorological elements such as humidity, wind speed, and topographic features, as well as variations in dust and vegetation coverage. These significantly affect the generation, accumulation, and dispersion of aerosols. Additionally, differences in population density, levels of economic development, and environmental protection policies contribute to the spatial heterogeneity in AOD observed across cities. The long-distance transport of regional pollutants creates complex interdependencies in AOD between cities.

Figure 14 shows the six-year (2018–2023) mean diurnal variation in the hourly AOD in cities located in the Beijing–Tianjin–Hebei region. As shown in Figure 14, except for the northernmost Zhangjiakou and Chengde with small variations, other cities in the Beijing–Tianjin–Hebei region have similar diurnal variations in the mean hourly AOD. Starting at 08:00 local time (00:00 UTC) (Figure 14a), the hourly AOD values first decrease to a trough around 11:00 local time (03:00 UTC) (Figure 14d), then gradually increase to a peak at approximately 13:00 local time (05:00 UTC) (Figure 14f). After that, the hourly AOD values gradually decrease until 18:00 local time (10:00 UTC) (Figure 14k), after which all cities show an increasing trend in the mean hourly AOD. The nocturnal increase in AOD not only reflects changes in physical dispersion conditions but also serves as a critical indicator of sustained emissions and chemical reactions.

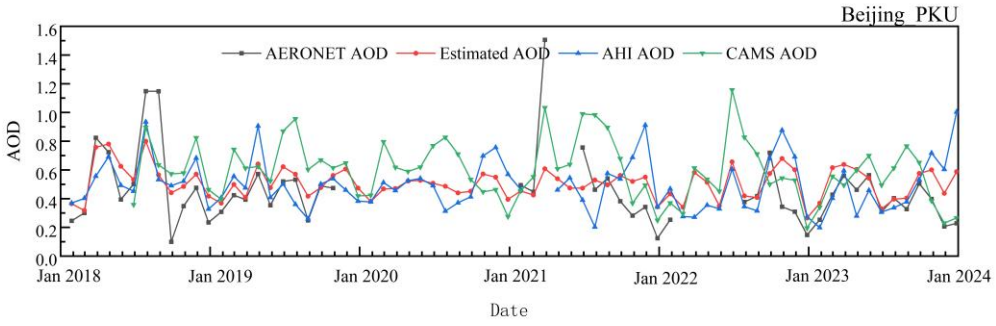
However, it should be noted that AOD represents the cumulative aerosol extinction effect from the ground to the top of the atmosphere. The nighttime variations observed in different cities are not solely indicative of changes in emission and chemical processes but are also associated with the vertical redistribution of aerosols. Enhanced surface radiative cooling during nighttime strengthens atmospheric stability, leading to a significant reduction in boundary layer height and increased concentration of aerosols in the lower troposphere. Due to higher aerosol concentrations within the boundary layer, low-level aerosols dominate optical extinction contributions, and their accumulation within the boundary layer significantly enhances columnar integrated extinction effects, thereby causing an increase in AOD. Simultaneously, the absence of strong convective activity during nighttime reduces horizontal pollutant dispersion, facilitating local pollutant accumulation. Additionally, continuous nighttime emissions from industrial production, heating systems, or transportation in certain cities elevate concentrations of aerosol precursor substances. These compounds may undergo chemical reactions to form secondary aerosols, further contributing to the rise in AOD values.



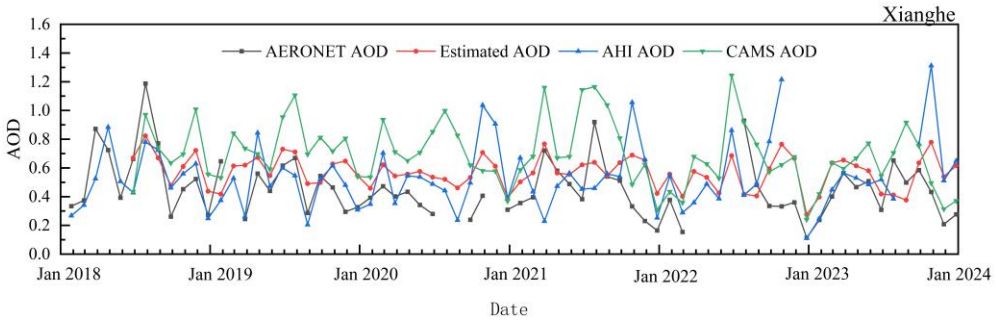
(**a**)



(**b**)



(**c**)



(**d**)

Figure 11. The monthly comparison of AERONET AOD, estimated AOD, AHI AOD, and CAMS AOD at four AERONET sites. (**a**) Beijing, (**b**) Beijing-CAMS, (**c**) Beijing_PKU, (**d**) Xianghe.

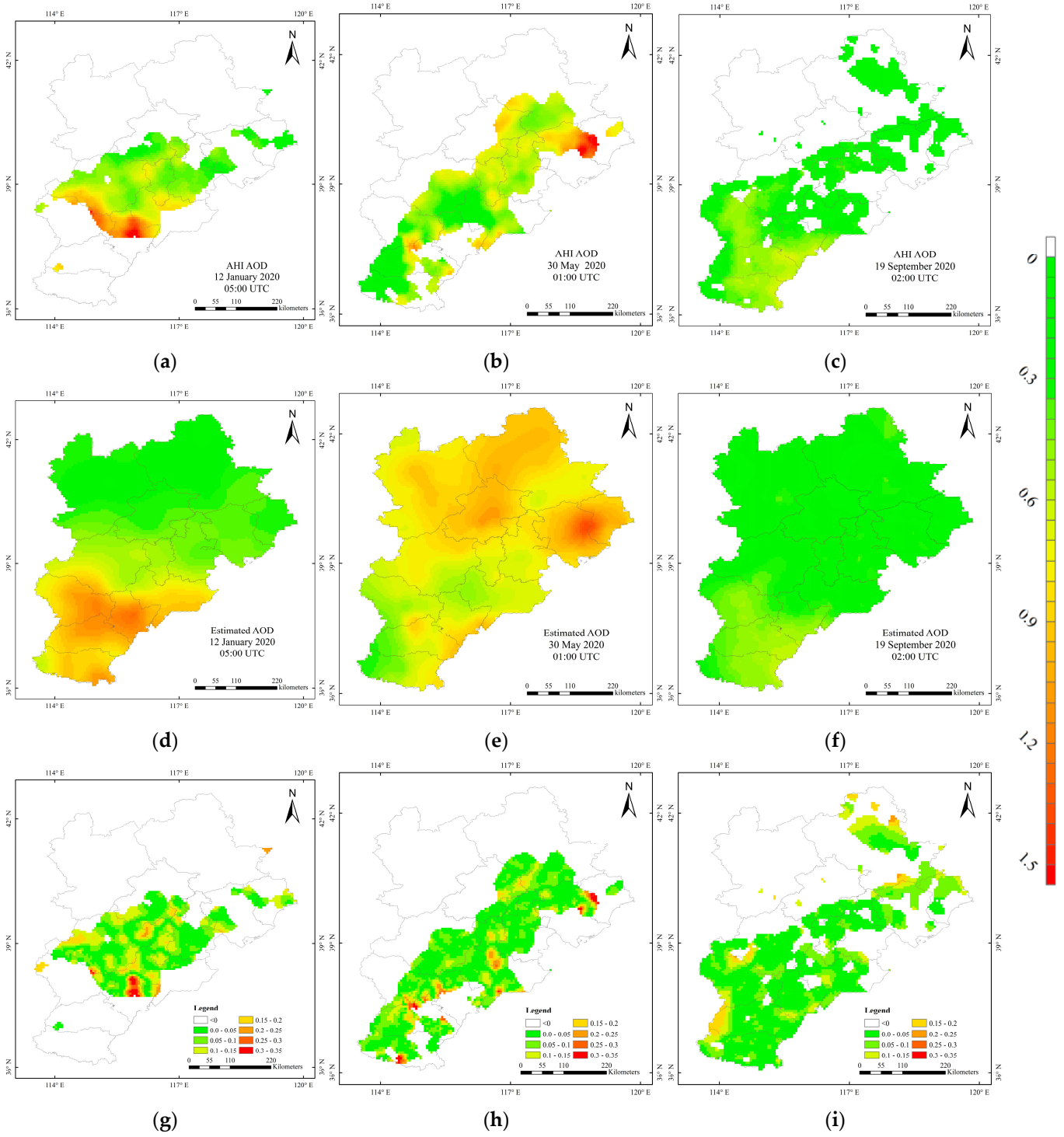


Figure 12. Spatial distribution and difference in AHI AOD and estimated AOD. (**a**–**c**) Spatial distribution of AHI AOD; (**d**–**f**) spatial distribution of estimated AOD; (**g**–**i**) absolute difference between AHI and the spatial distribution of estimated AOD.

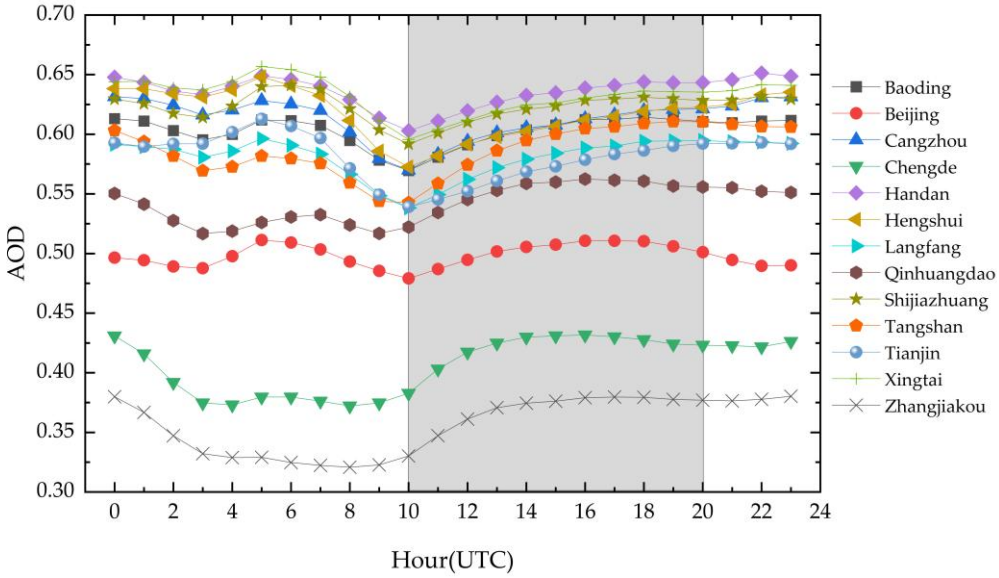


Figure 13. Change in AOD hourly average of cities in BTH from 2018 to 2023. (Gray Area: The range of nighttime hours in the study area).

3.3.2. Seasonal Averages

Figure 15 shows the seasonal average of estimated AOD in BTH from 2018 to 2023. As illustrated in Figure 15, AOD in the BTH has obvious seasonal characteristics. The spring and autumn AOD averages are significantly higher than those in other seasons. Spring is the season with frequent dust events in northern China. The BTH region is greatly affected by the transport of dust from surrounding arid and semi-arid regions (e.g., the Mongolian Plateau and the northwestern provinces of China), and the superimposed effect of local pollution sources results in high AOD levels. Summer has the lowest average AOD because of the favorable meteorological conditions during the rainy season. Frequent precipitation effectively removes aerosol particles from the atmosphere via wet deposition. Meanwhile, strong vertical diffusion of aerosols caused by active atmospheric convection under high-temperature backgrounds in summer also contributes to low AOD. Higher AOD values were found in autumn in the south areas with intense farmland cultivation due to the increase in aerosol emissions from straw burning and farmland operations. Furthermore, the activity of weak cold air results in stable atmospheric conditions during the autumn months, which hampers the dispersion of pollutants and encourages the buildup of aerosols within the area. On the contrary, regional average AOD was relatively low in winter. This is mainly attributed to the effects of the Mongolian High and the winter monsoon, whose northwest-to-southeast air flow inhibited an increase in aerosol concentration.

3.3.3. Annual Average

Figure 16 shows the annual average AOD distribution in BTH from 2018 to 2023. Figure 16 indicates that the spatial distribution of AOD displays a prominent “C”-shaped pattern, delineated by a dividing line traversing Tangshan, Beijing, Baoding, Shijiazhuang, Xingtai, and Handan. Areas to the north exhibit low AOD values, while those in the south demonstrate high AOD values. Notably, this spatial distribution closely correlates with the region’s topographic elevation patterns.

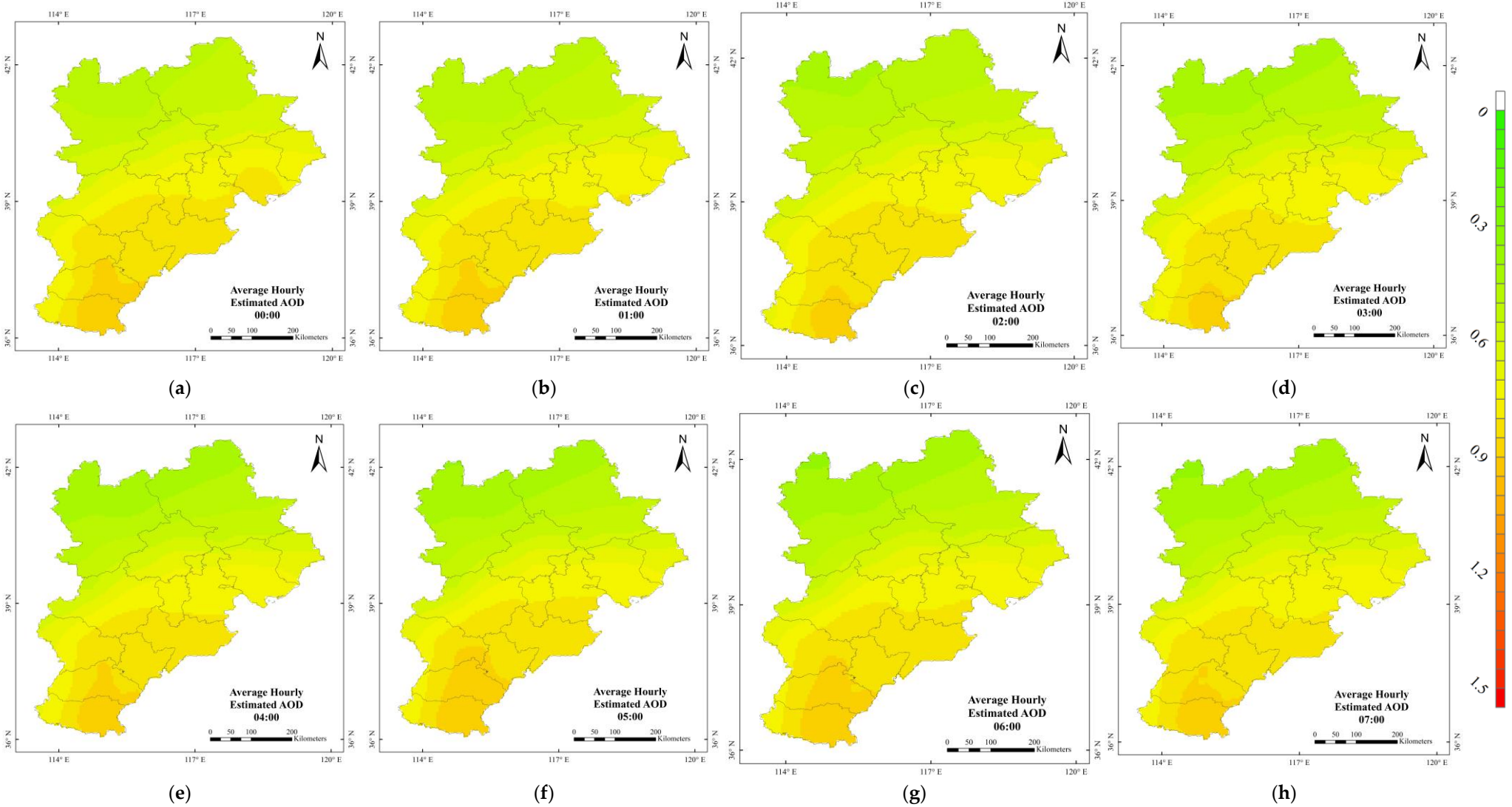


Figure 14. *Cont.*

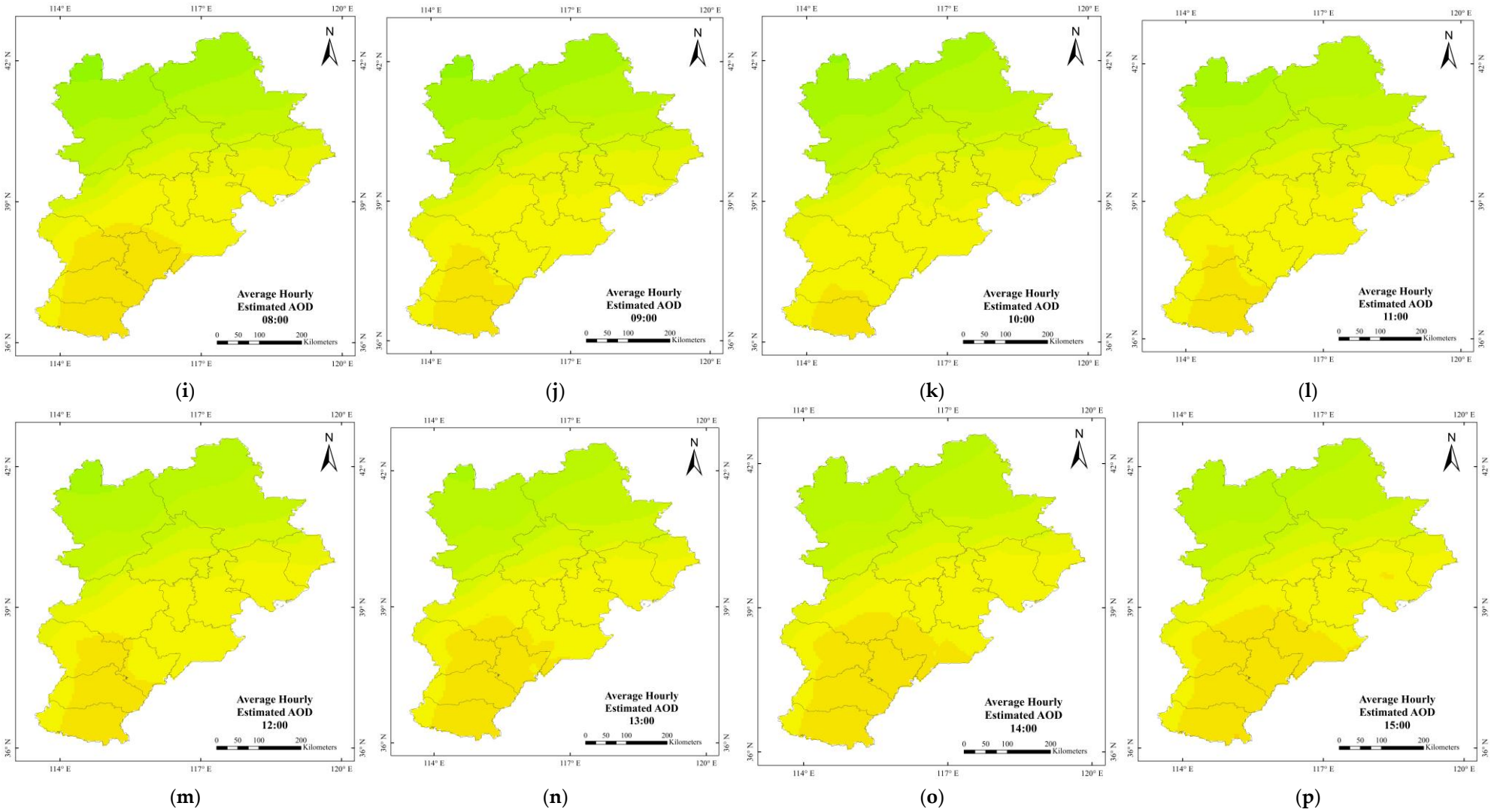


Figure 14. *Cont.*

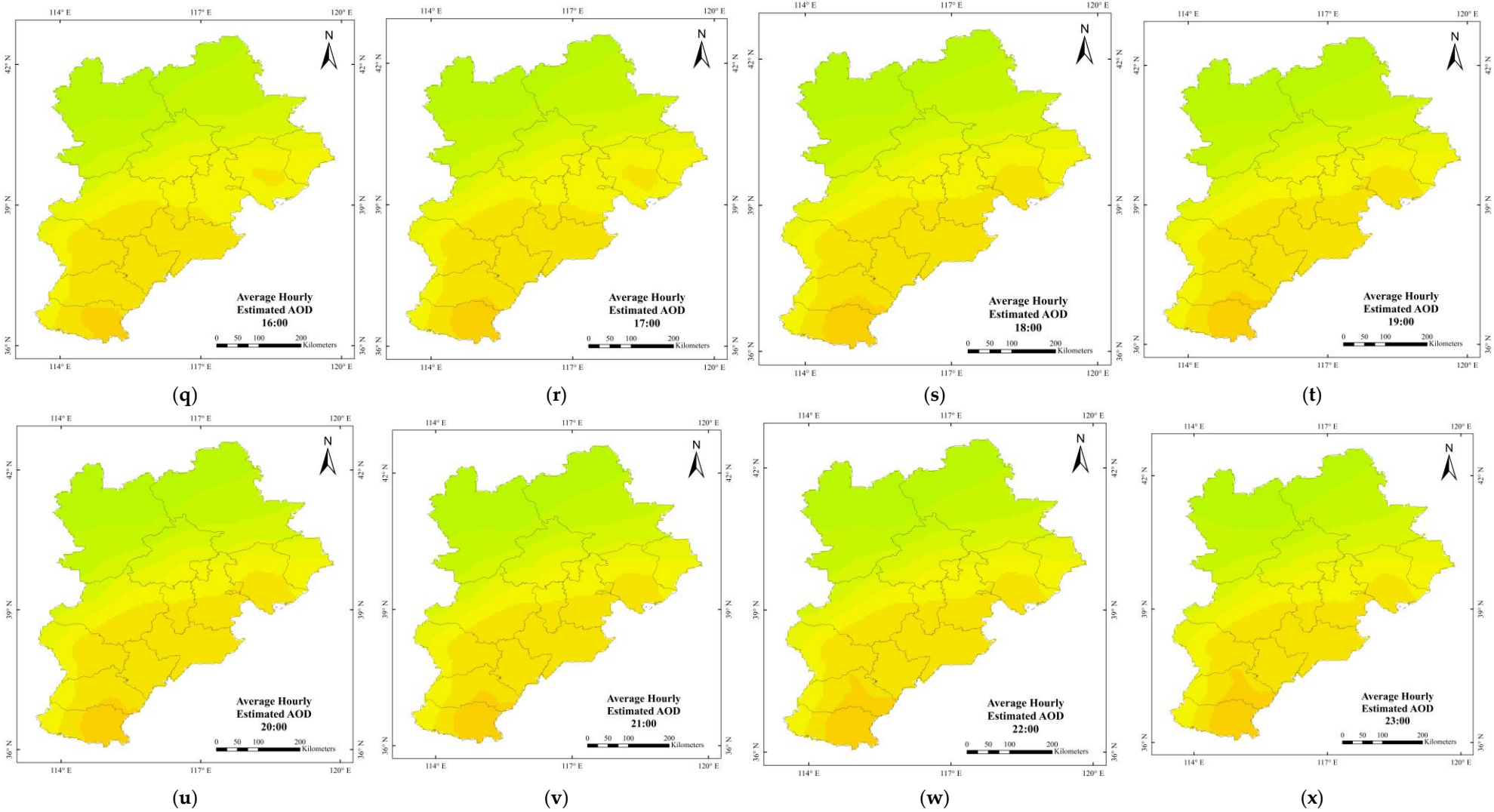


Figure 14. Spatial distribution of AOD hourly mean from 2018 to 2023. (**a**–**x**): 00:00 UTC–23:00 UTC.

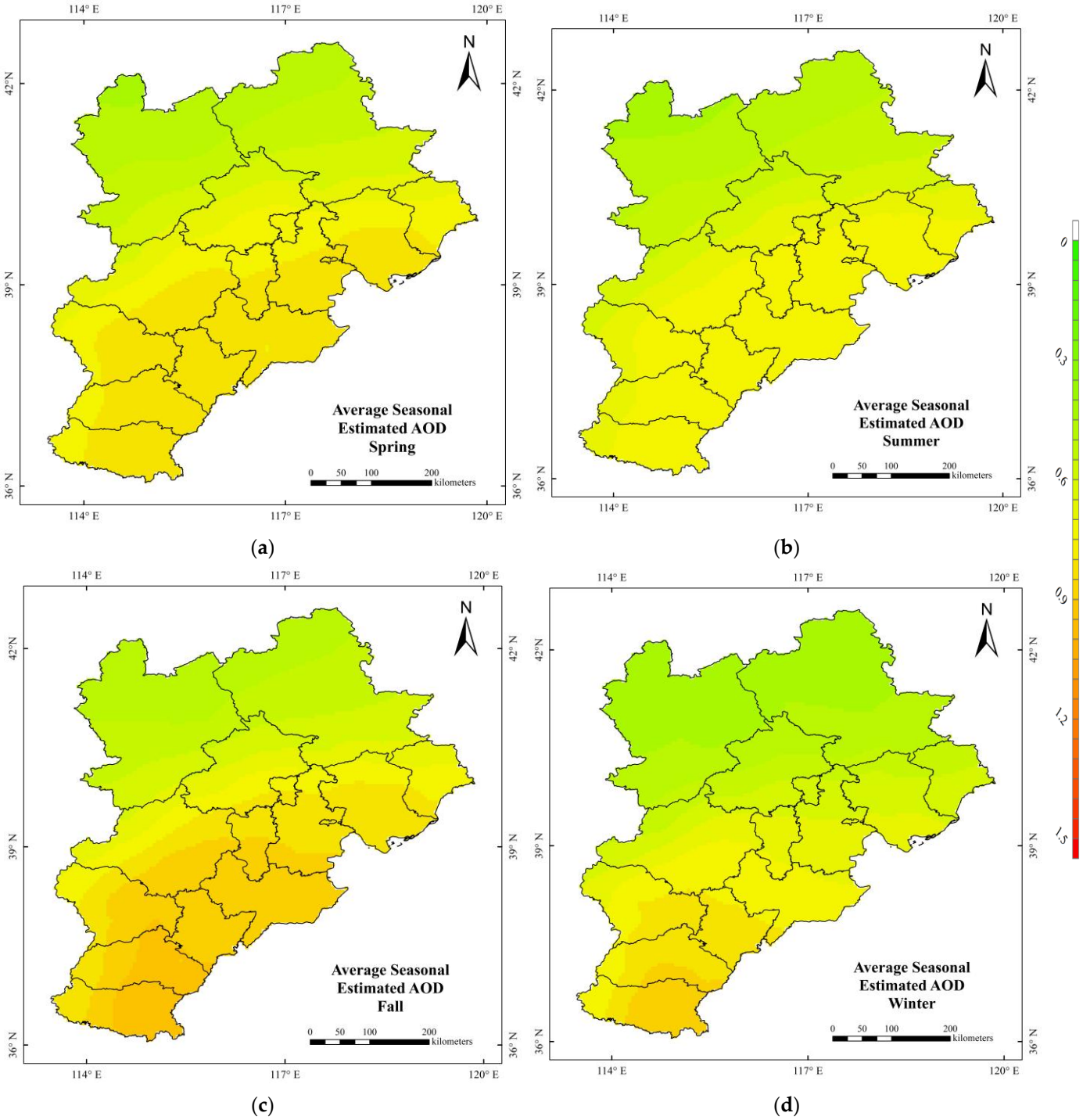


Figure 15. Seasonal average of estimated AOD in BTH from 2018 to 2023. (**a**) Spring, (**b**) summer, (**c**) autumn, (**d**) winter.

The graph indicates a consistent decline in AOD from 2018 to 2023, signaling a significant enhancement in regional air quality. However, minor fluctuations in AOD were observed in 2021 (Figure 16d) and 2023 (Figure 16f). This overall improvement can largely be attributed to the stringent enforcement of air pollution control policies by national and local governments in recent years. It is important to note that the COVID-19 pandemic in 2020 had a unique impact on AOD trends. The restrictions and lockdowns significantly diminished human activities, industrial production, and transportation, resulting in a subsequent decrease in pollutant emissions. As a result, AOD levels temporarily declined. The AOD values in BTH reached a low point, leading to a substantial improvement in

air quality in the short term. However, as the pandemic situation eased in 2021 and 2023, socioeconomic activities resumed. This led to an increase in industrial production and transportation intensity, causing a rise in pollutant emissions and a slight rebound in AOD values.

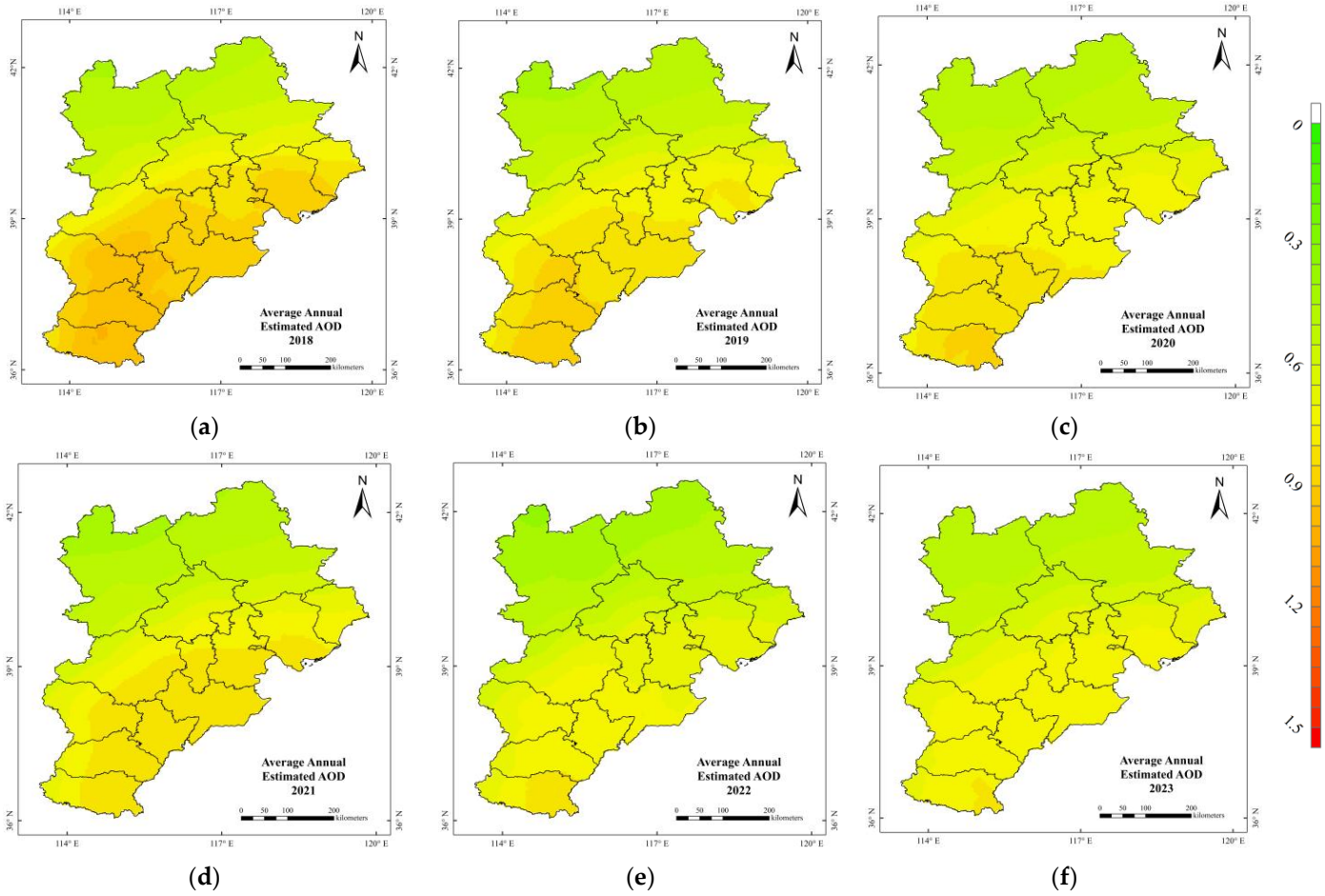


Figure 16. Annual average distribution of AOD in BTH from 2018 to 2023. (**a**) 2018; (**b**) 2019; (**c**) 2020; (**d**) 2021; (**e**) 2022; (**f**) 2023.

4. Discussion

Existing nighttime AOD inversion methods are primarily categorized into two approaches: one based on low-light remote sensing data for AOD retrieval and the other utilizing AERONET ground station observations. The first approach mainly employs DMSP/OLS or VIIRS/DNB data, using artificial light sources or moonlight as radiation sources to conduct nighttime AOD estimation research. However, this method faces limitations due to lower radiative energy received by satellite sensors during nighttime and its sensitivity to light source conditions, resulting in restricted applicability in areas with no or weak light sources. The second approach estimates nighttime AOD through AERONET observational data, which demonstrates better physical reliability. Nevertheless, this method suffers from insufficient spatial coverage caused by limited AERONET station numbers, with only a few stations providing usable data and even fewer capable of supplying nighttime AOD observations. In the BTH region, there are only four AERONET sites, which are primarily concentrated in and around the Beijing area, making it difficult to provide observational data for other regions located further away. Moreover, among these four stations, only two are capable of providing partial nocturnal observational data.

In contrast, this study does not directly rely on nighttime low-light data or sparse AERONET nighttime AOD observations. Instead, we establish a day-and-night AOD estimation model by integrating ground-based air quality monitoring data with AHI AOD products. Through machine learning techniques that extract and learn underlying correlation patterns, we generate AOD datasets for the BTH region from 2018 to 2023. Comparative evaluations between retrieved AOD values and both AHI AOD and AERONET AOD demonstrate improved continuity, completeness, and regional applicability of nighttime AOD data.

The model's evaluation was conducted using both ten-fold cross-validation and leave-one-city-out cross-validation, and the results consistently demonstrated high R^2 values and low RMSE values. Even though the estimation precision was slightly lower in certain eco-type cities, the overall performance of the model remained exceptional. A comparative analysis of daytime and nighttime AERONET measurements from the Beijing_PKU and Beijing-CAMS locations further confirmed the model's reliability. This analysis revealed a significant increase in both the coverage and volume of AOD data. Remarkably, the analysis showed that nighttime estimation errors were comparable to those made during the day, with both remaining at minimal levels. This highlights the model's high accuracy and temporal consistency. Furthermore, the estimated AOD displayed robust spatiotemporal consistency with existing satellite AOD products, thereby validating the model's robustness in regional AOD estimation.

In order to assess the versatility of the all-day AOD estimation model in relation to unique events, we examined two specific cases: a dust storm outbreak and the Spring Festival period of 2021. Figure 17 depicts a dust storm event that transpired from 18 March to 19 March 2023. Between 16:00 and 20:00 UTC on March 18, pollutants gathered in the southwestern region of the BTH. By 21:00 UTC, the dust had begun to disperse northward, causing the polluted area to gradually expand. The spatial distribution of AOD clearly indicated a distinct transmission path. From 21:00 UTC on 18 March to 15:00 UTC on 19 March, contaminants were spread across the entire BTH region. Regional AOD levels significantly increased, highlighting the extensive impact of the dust storm. The all-day AOD estimation model effectively captured the formation and spread of the dust storm event, particularly in terms of its temporal and spatial details. This validates the model's suitability for monitoring special events and its capacity to track regional aerosol dynamics in near real-time.

Figure 18 depicts the pollution event that occurred during the Spring Festival period, from 11 February 2021 (Lunar New Year's Eve) to 12 February 2021 (the Spring Festival). The figure illustrates that aerosol particles began to accumulate in the atmosphere at 10:00 UTC on 11 February 2021, which is likely attributable to the significant emissions from holiday celebrations, including fireworks. High AOD levels persisted from 10:00 UTC on 11 February 2021 to 08:00 UTC on 12 February 2021, with pollution concentrations remaining elevated throughout this period. However, the AOD value notably decreased at 09:00 UTC on 12 February 2021. The all-day AOD estimation model effectively tracked the pollution dynamics during the Spring Festival, adeptly capturing the rapid accumulation and subsequent gradual dissipation of pollutants.

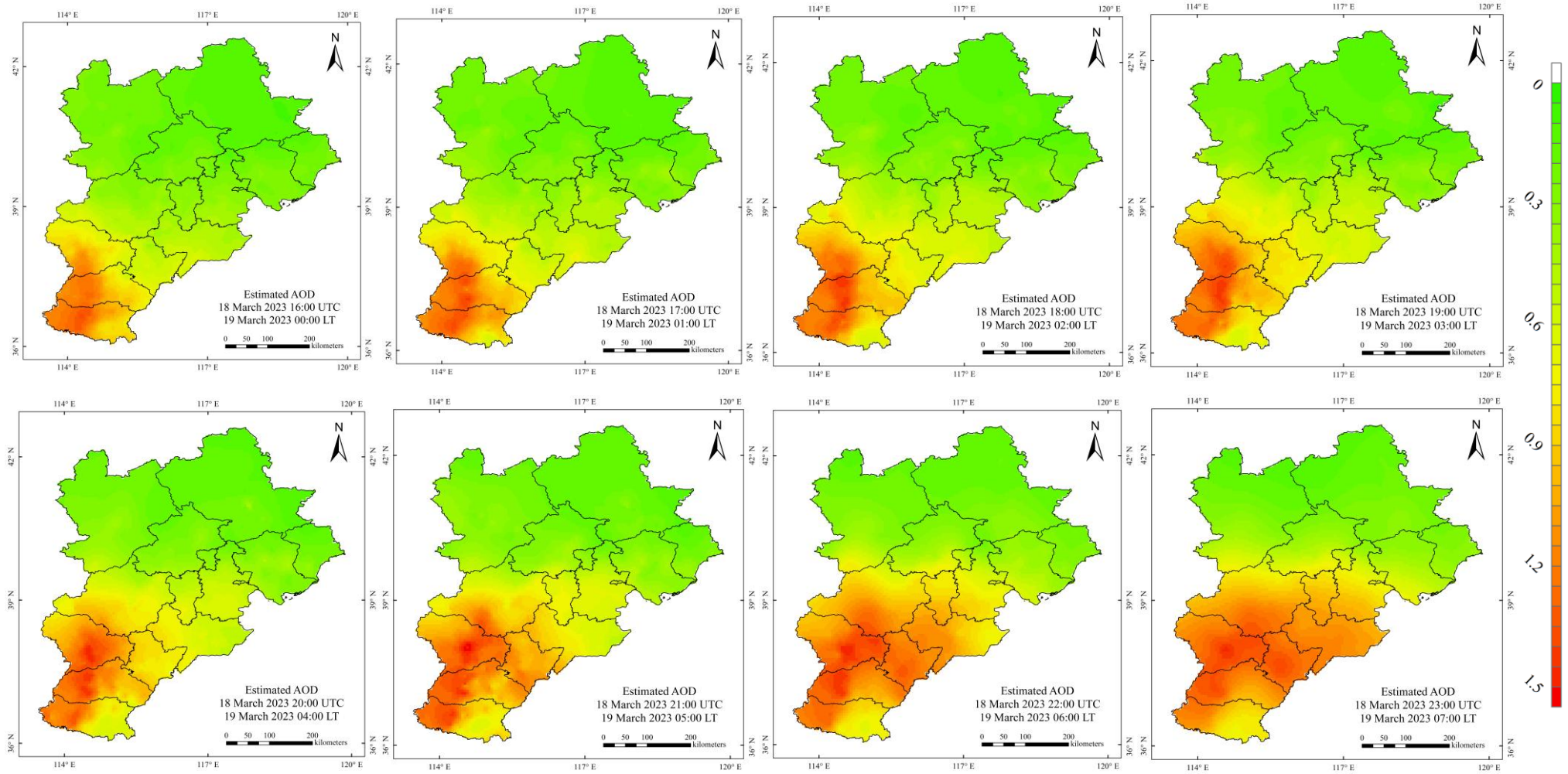


Figure 17. *Cont.*

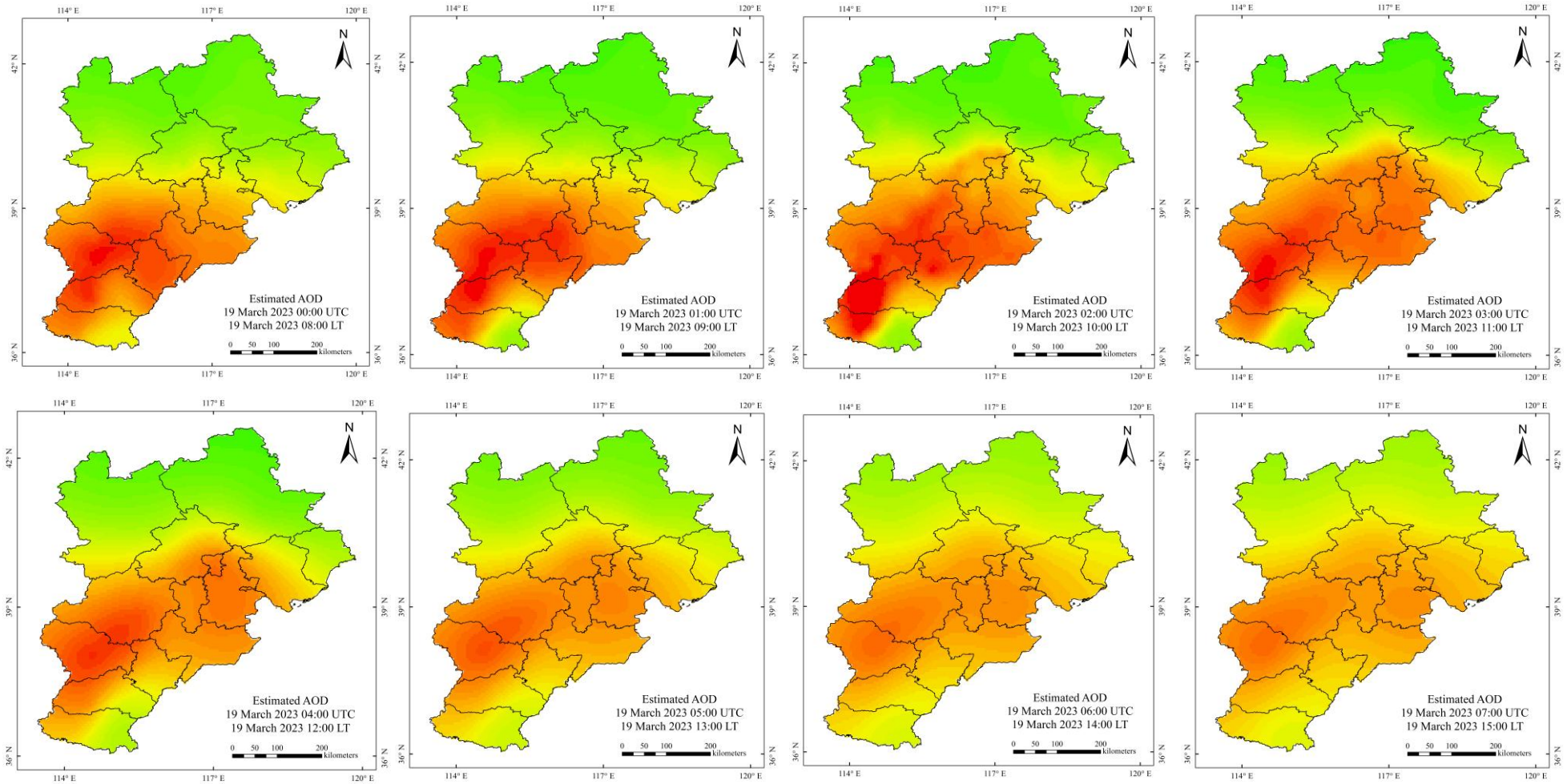


Figure 17. *Cont.*

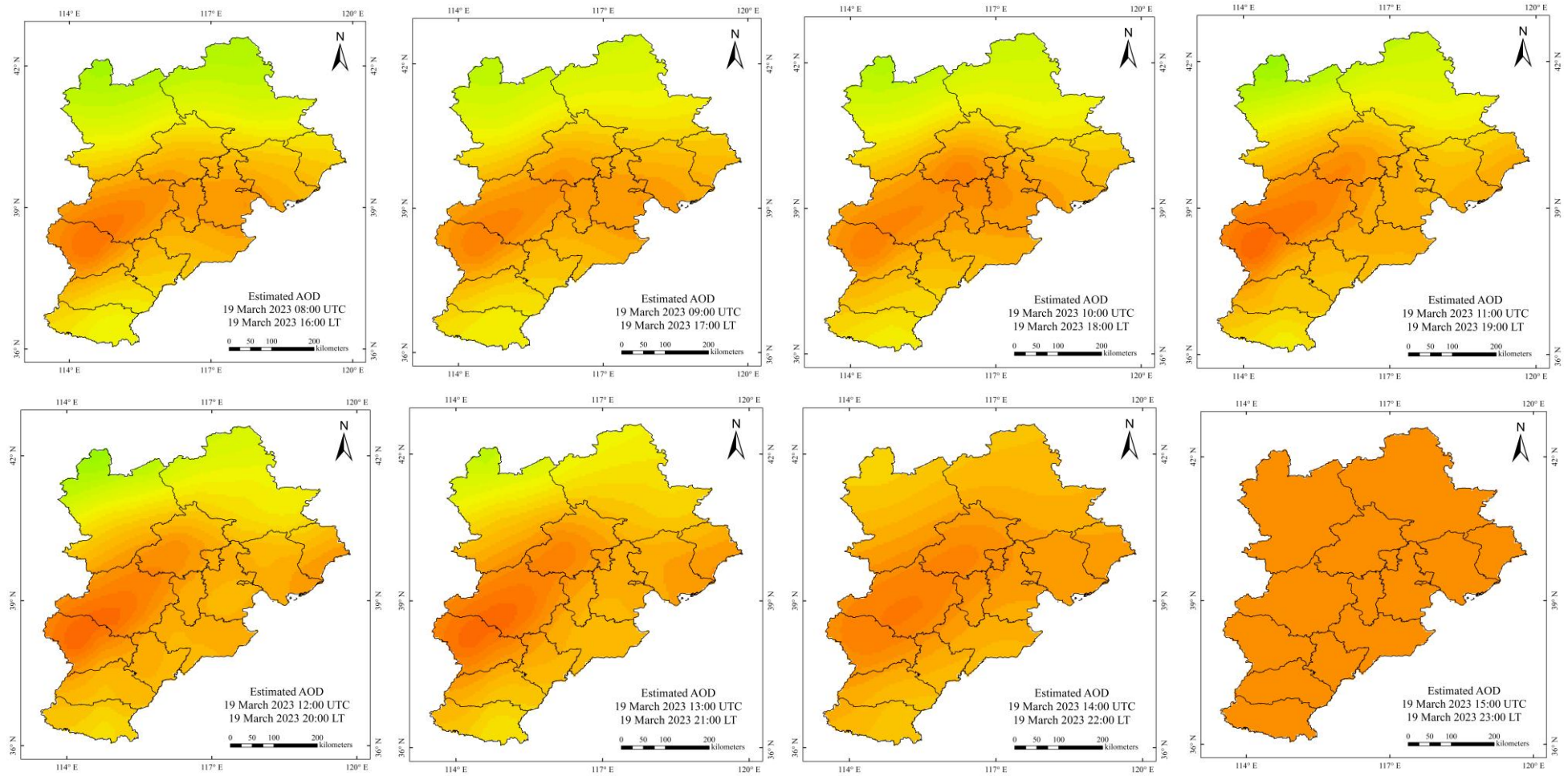


Figure 17. A dust storm broke out from 18 March to 19 March 2023.

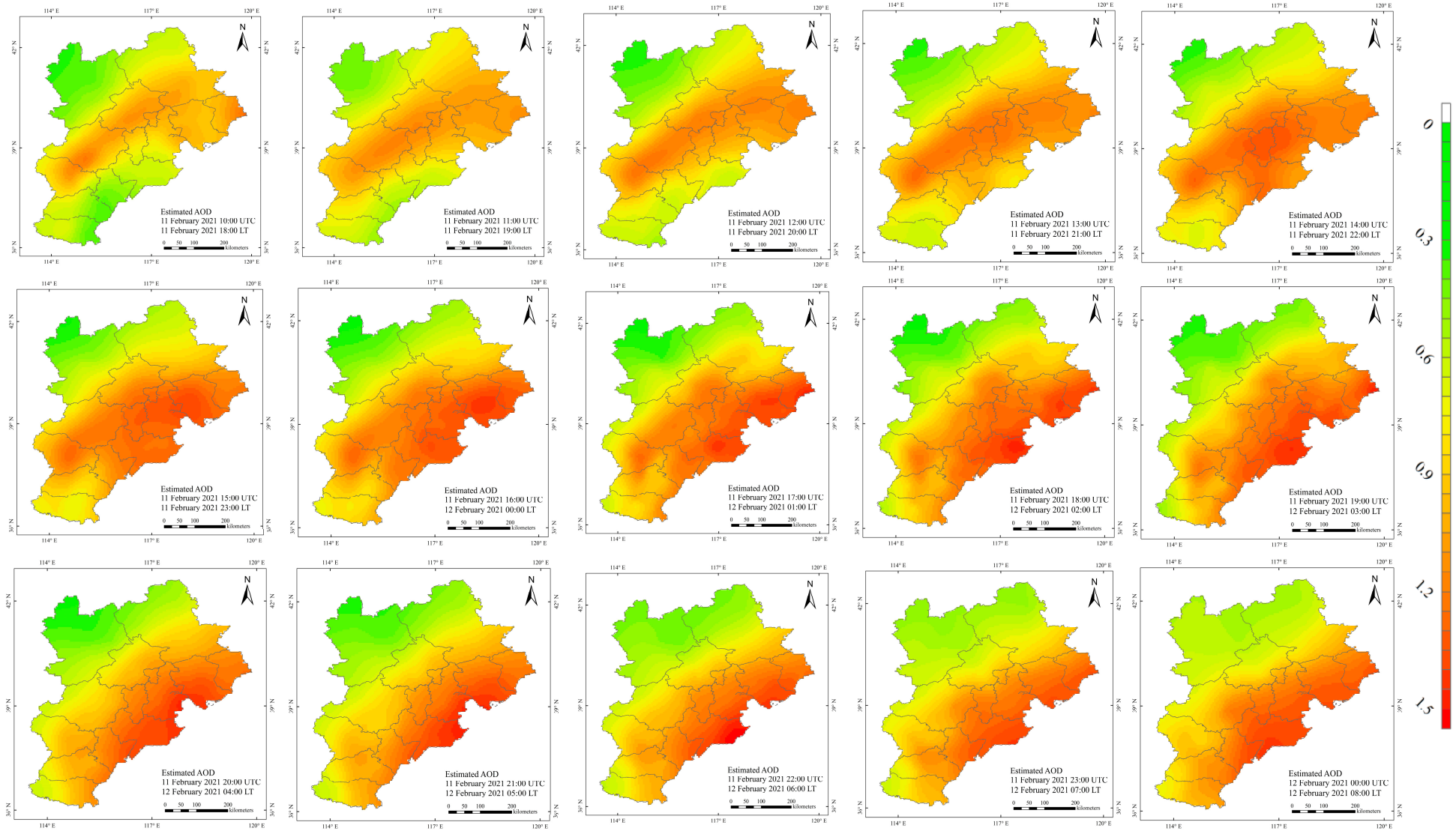


Figure 18. *Cont.*

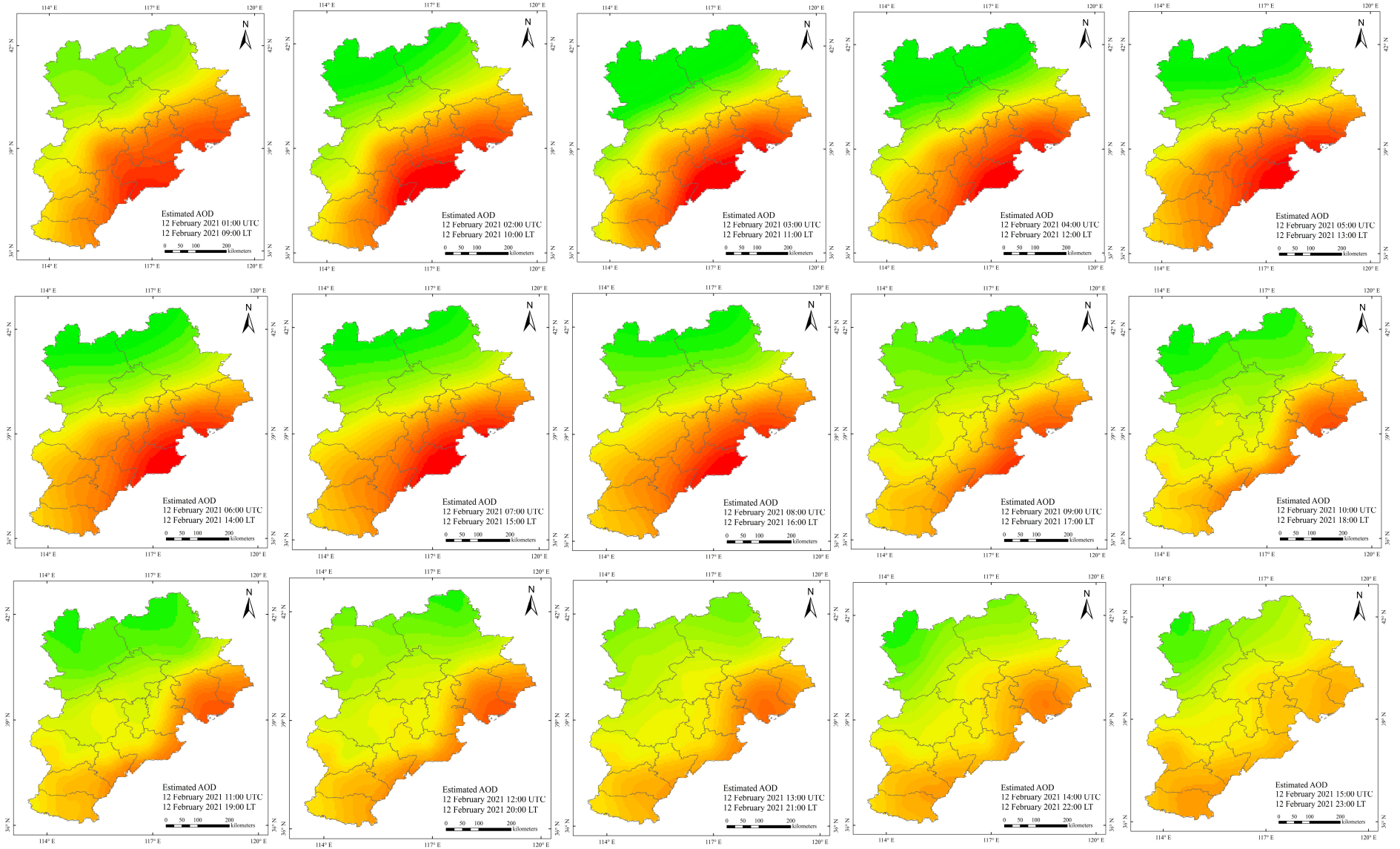


Figure 18. Spring Festival pollution process from 11 February 2021 to 12 February 2021.

Despite the strong performance of the proposed all-day AOD estimation model, this study is subject to several limitations. Firstly, the research relies on satellite remote sensing, ground monitoring, meteorological, and geographic data. The disparities in spatial and temporal resolution and quality among these data sources could potentially introduce inconsistencies in the estimation results. Secondly, due to the unavailability of AHI AOD data at nighttime and the limited availability of nocturnal AOD observations from AERONET, this study employs a daytime dataset to train the model for application in nighttime AOD estimation. The Taylor diagram illustrates model performance by comprehensively displaying the relationships between AOD estimates and observational data correlation parameters. The analysis of AOD estimates against AERONET AOD (Appendix C, Figure A1a) using Taylor diagrams, combined with results from two validation methods comparing AOD estimates and AHI AOD (Appendix C, Figure A1b,c), reveals that the model performs well in most regions. However, under both the leave-one-site-out and sample cross-validation approaches, the overall standard deviation remains low, indicating a certain smoothing effect in characterizing AOD variations. The model demonstrates lower accuracy in certain ecological cities or less-polluted areas, which is manifested as scattered distributions in the Taylor diagram. This discrepancy may be attributed to insufficient representation of aerosol characteristics from these regions in the training dataset, suggesting the model's sensitivity to sample composition and regional characteristics. Lastly, the incorporation of seasonal variations in AOD and its complex interactions with human activities presents significant challenges to the model. To address these limitations, future research should focus on enhancing the quality and scope of data, expanding the model's applicability, reducing local estimation inaccuracies, and incorporating the impacts of external environmental variables.

5. Conclusions

In this study, we developed a comprehensive diurnal model to estimate atmospheric optical depth (AOD) by harnessing satellite remote sensing data, ground-level air quality monitoring records, multi-level atmospheric data, and geographic information. The primary objective of this model was to evaluate the spatiotemporal distribution of AOD in the BTH region from 2018 to 2023. We present our findings as follows:

1. The model exhibited high accuracy, as evidenced by the results from sample cross-validation and leave-one-city-out cross-validation methods. In the case of sample cross-validation, the model achieved R^2 values above 0.96 and RMSE values below 0.1. Similarly, the leave-one-city-out cross-validation method resulted in R^2 values exceeding 0.8 and RMSE values under 0.2.
2. Compared to existing AOD products, the R^2 value for daytime estimated AOD in relation to AERONET AOD was 0.622 with an RMSE of 0.252. For nighttime estimated AOD against AERONET AOD, the R^2 was calculated to be 0.651, with a corresponding RMSE of 0.223. Notably, the difference between the estimated AOD and that obtained from AERONET was predominantly within the range of -1 to 1. The minimal estimation error underscored the stability and reliability of the derived AOD.
3. The annual mean AOD generally decreased with intermittent increases from 2018 to 2023, reflecting both sustained decline and short-term variability. The AOD in the BTH showed notable seasonal changes, displaying elevated levels during spring and autumn, while summer and winter recorded decreased values. The diurnal variation in AOD initially decreased during the day, then increased and decreased again, and finally increased at night.

In conclusion, the all-day AOD estimation model formulated in this research presents a robust tool for monitoring air quality and enabling early warnings in the BTH region. Furthermore, this study contributes crucial scientific data to be utilized in future research on aerosols, strategies for pollution prevention, and environmental management decisions.

Author Contributions: Writing—original draft, J.Y., B.Z. and Y.Y.; conceptualization and methodology, S.L. and W.Z.; validation, formal analysis, and data curation, S.L. and W.Z.; writing—review and editing, all authors; investigation, B.L.; supervision, W.Z. and X.Y.; funding acquisition, W.Z. and S.L.; and project administration, B.L. All authors have read and agreed to the published version of the manuscript.

Funding: This research was supported by the Hebei Natural Science Foundation (Grant No. D2024409002) and by the Department of Science and Technology of Hebei Province under the Central Guidance of Local Science and Technology Development Funds Project (Grant No. 246Z7602G).

Institutional Review Board Statement: Not applicable.

Informed Consent Statement: Not applicable.

Data Availability Statement: The data provided in this study are available upon request from the corresponding author. The data are not publicly available as they are being collated.

Acknowledgments: We would like to thank the China National Environmental Monitoring Center for providing ground-level air quality data, the European Centre for Medium-Range Weather Forecasts for reanalysis meteorological data, the Aerosol Robotic Network for AERONET AOD, and the Japan Aerospace Exploration Agency for AHI AOD. We also sincerely thank all anonymous reviewers for their efforts.

Conflicts of Interest: The authors declare no conflict of interest.

Abbreviations

The following abbreviations are used in this manuscript:

BTH	Beijing–Tianjin–Hebei
AOD	Aerosol optical depth
AERONET	Aerosol Robotic Network
AHI	Advanced Himawari Imager
ECMWF	European Centre for Medium-Range Weather Forecasts
U10	10 m u-component of wind
V10	10 m u-component of wind
SP	Surface pressure
BLH	Boundary layer height
T2M	2 m temperature
RH	Relative humidity
T	Temperature
U	U-component of wind
V	V-component of wind
JAXA	Japan Aerospace Exploration Agency
NDVI	Normalized Difference Vegetation Index
CMG	Climate Modeling Grid
SRTM	Shuttle Radar Topography Mission
UTC	Coordinated Universal Time
GBDT	Gradient boosting decision tree

Appendix A

Table A1 provides the annual mean $PM_{2.5}$ concentrations for cities in the BTH region from 2018 to 2023. These data supplement the main text by giving detailed yearly values for each city, which are essential for understanding temporal trends and spatial patterns in air pollution across the region. Including this table in the appendix ensures that the flow of the main text is not disrupted while still providing all information necessary to reproduce and interpret the study's findings.

Table A1. Annual average $PM_{2.5}$ concentration (micrograms per cubic meter) in the Beijing–Tianjin–Hebei region from 2018 to 2023.

2018	2019	2020	2021	2022	2023
Zhangjiakou (29)	Zhangjiakou (25)	Zhangjiakou (23)	Zhangjiakou (23)	Zhangjiakou (17)	Zhangjiakou (18)
Chengde (32)	Chengde (29)	Chengde (27)	Chengde (30)	Chengde (26)	Chengde (25)
Qinhuangdao (38)	Qinhuangdao (41)	Qinhuangdao (34)	Beijing (33)	Qinhuangdao (28)	Qinhuangdao (31)
Beijing (51)	Beijing (42)	Beijing (38)	Qinhuangdao (34)	Beijing (30)	Beijing (32)
Langfang (52)	Langfang (46)	Langfang (42)	Langfang (37)	Langfang (36)	Tangshan (40)
Tianjin (52)	Changzhou (50)	Changzhou (47)	Tianjin (39)	Tangshan (37)	Langfang (40)
Changzhou (59)	Tianjin (51)	Tianjin (48)	Changzhou (40)	Tianjin (37)	Tianjin (41)
Tangshan (60)	Tangshan (54)	Tangshan (49)	Hengshui (42)	Changzhou (39)	Shijiazhuang (44)
Hengshui (62)	Hengshui (56)	Baoding (50)	Baoding (43)	Baoding (43)	Baoding (44)
Baoding (67)	Baoding (58)	Hengshui (52)	Tangshan (43)	Hengshui (43)	Hengshui (44)
Xingtai (69)	Shijiazhuang (63)	Xingtai (53)	Xingtai (43)	Shijiazhuang (46)	Changzhou (44)
Handan (69)	Xingtai (65)	Handan (57)	Handan (46)	Xingtai (48)	Xingtai (45)
Shijiazhuang (72)	Handan (66)	Shijiazhuang (58)	Shijiazhuang (46)	Handan (51)	Handan (47)

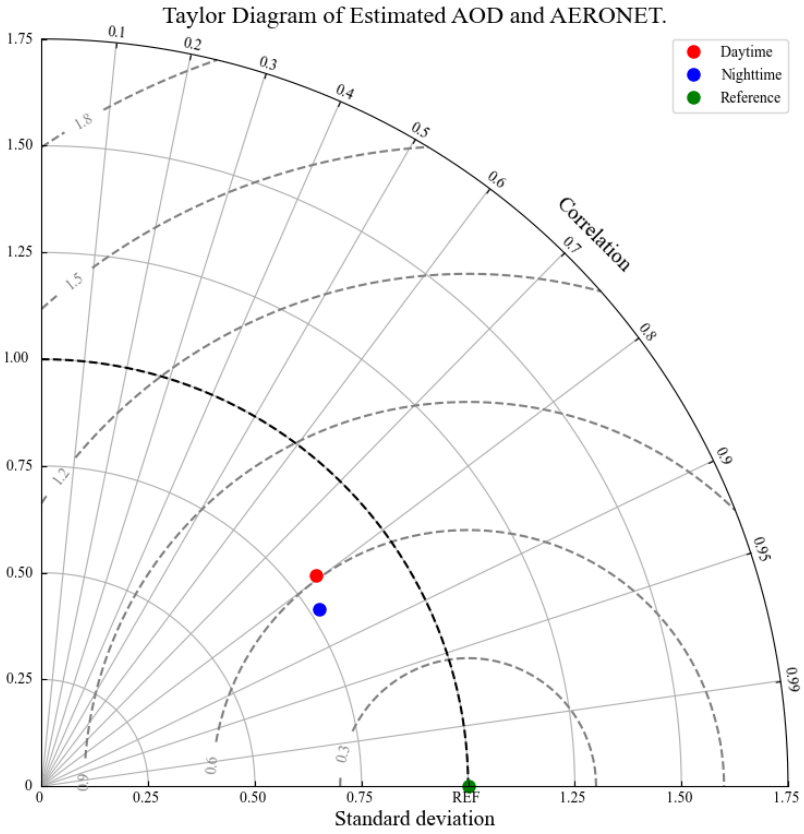
Appendix B

Table A2. All-day AOD estimation model hyperparameter data.

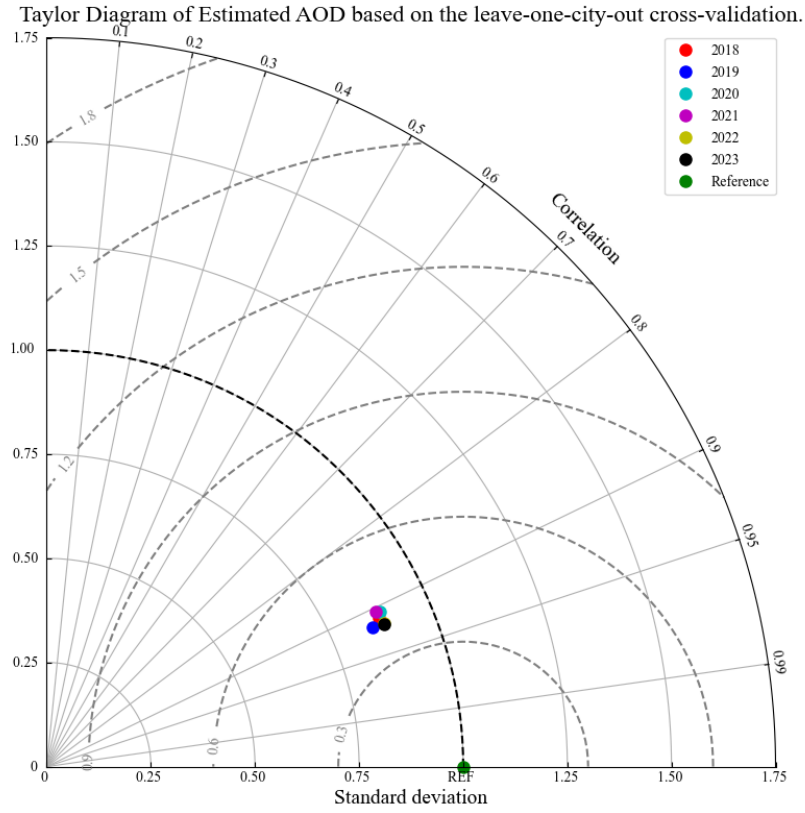
Parameter / Year	N_Estimators	Max_Depth	Learning_Rate	Min_Child_Weight
2018	341	28	0.0914	23.8111
2019	365	30	0.0748	4.6974
2020	339	27	0.2122	3.0407
2021	337	25	0.1530	23.8375
2022	332	21	0.0277	10.7043
2023	332	21	0.0277	10.7043

Appendix C

Figure A1 shows the Taylor diagram generated based on the correlation data. Figure A1a presents the Taylor diagram of AOD estimates in the BTH region from 2018 to 2023 against AERONET AOD correlation parameters. Figure A1b shows the annual all-daytime AOD estimation models' Taylor diagrams for the BTH region from 2018 to 2023, based on the leave-one-city-out cross-validation method. Figure A1c illustrates the annual all-daytime AOD estimation models' correlation parameter Taylor diagrams for the BTH region from 2018 to 2023, using the sample cross-validation method.

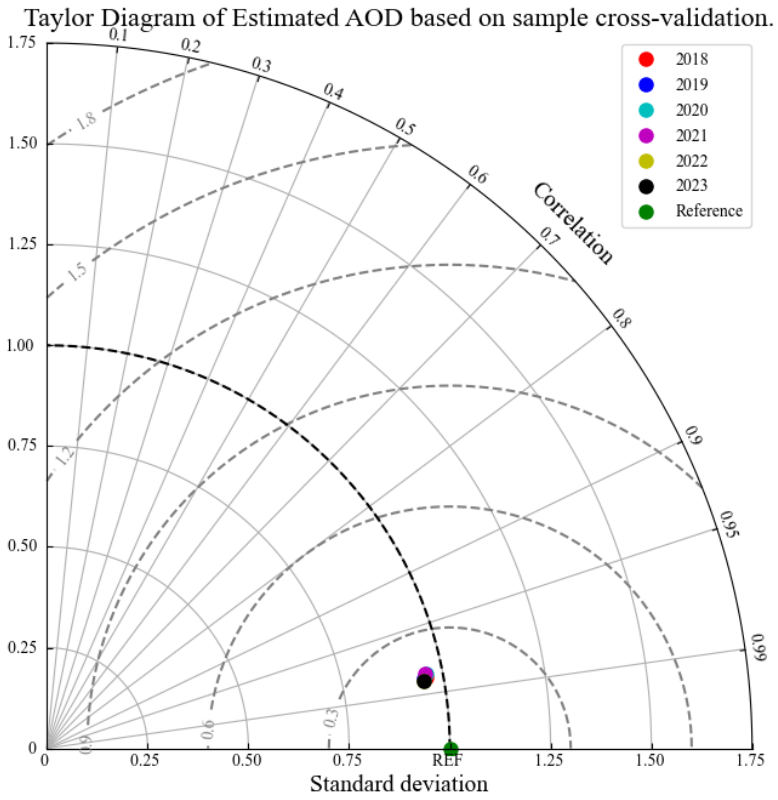


(**a**)



(**b**)

Figure A1. *Cont.*



(**c**)

Figure A1. Taylor diagram of correlation coefficients and RMSE parameters. (**a**) Comparison of estimated AOD with AERONET AOD in the BTH region (2018–2023), (**b**) Taylor diagrams of annual all-day AOD estimation models based on leave-one-city-out cross-validation, (**c**) Taylor diagrams of correlation coefficients for annual all-day AOD estimation models using sample-based cross-validation.

References

1. Peng, J.; Hu, M.; Shang, D.; Wu, Z.; Du, Z.; Tan, T.; Wang, Y.; Zhang, F.; Zhang, R. Explosive Secondary Aerosol Formation during Severe Haze in the North China Plain. *Environ. Sci. Technol.* **2021**, *55*, 2189–2207. [CrossRef] [PubMed]
2. IPCC. *Climate Change 2007: Mitigation of Climate Change*; Cambridge University Press: Cambridge, UK, 2007. [CrossRef]
3. Xie, Y. Development of Hourly AOD Dataset Based on Geostationary Satellites and Fusion of Multi-Source AOD Datasets. Master's Thesis, Chinese Academy of Sciences (Institute of Remote Sensing and Digital Earth), Beijing, China, 2019. Available online: https://d.wanfangdata.com.cn/thesis/Y3600084 (accessed on 7 January 2026).
4. Barreto, Á.; Cuevas, E.; Granados-Muñoz, M.-J.; Alados-Arboledas, L.; Romero, P.M.; Gröbner, J.; Kouremeti, N.; Almansa, A.F.; Stone, T.; Toledano, C.; et al. The New Sun-Sky-Lunar Cimel CE318-T Multiband Photometer—A Comprehensive Performance Evaluation. *Atmos. Meas. Tech.* **2016**, *9*, 631–654. [CrossRef]
5. Giles, D.M.; Slutsker, I.; Schafer, J.; Sorokin, M.G.; Smirnov, A.; Eck, T.F.; Holben, B.; Welton, E.J. Uncertainty and Bias in AERONET Nighttime AOD Measurements. In Proceedings of the AGU Fall Meeting Abstracts; 1 December 2019; Volume 2019, p. A23R-3050. Available online: https://ui.adsabs.harvard.edu/abs/2019AGUFM.A23R3050G (accessed on 15 December 2025).
6. Zhang, W.; Liu, S.; Chen, X.; Mi, X.; Gu, X.; Yu, T. Estimation of All-Day Aerosol Optical Depth in the Beijing–Tianjin–Hebei Region Using Ground Air Quality Data. *Remote Sens.* **2024**, *16*, 1410. [CrossRef]
7. Mishchenko, M.I.; Geogdzhayev, I.V.; Cairns, B.; Carlson, B.E.; Chowdhary, J.; Lacis, A.A.; Liu, L.; Rossow, W.B.; Travis, L.D. Past, Present, and Future of Global Aerosol Climatologies Derived from Satellite Observations: A Perspective. *J. Quant. Spectrosc. Radiat. Transf.* **2007**, *106*, 325–347. [CrossRef]
8. Wei, X.; Chang, N.B.; Bai, K.; Gao, W. Satellite Remote Sensing of Aerosol Optical Depth: Advances, Challenges, and Perspectives. *Crit. Rev. Environ. Sci. Technol.* **2020**, *50*, 1640–1725. [CrossRef]

9. Ma, Y.; Zhang, W.; Zhang, L.; Wu, Y.; Tang, J.; Fu, Y. Research Progress of Atmospheric Remote Sensing Based on Satellite Nighttime Low-Light Data. *J. Atmos. Environ. Opt.* **2024**, *19*, 125–141. [CrossRef]
10. Barreto, Á.; Román, R.; Cuevas, E.; Berjón, A.J.; Almansa, A.F.; Toledano, C.; González, R.; Hernández, Y.; Blarel, L.; Goloub, P.; et al. Assessment of Nocturnal Aerosol Optical Depth from Lunar Photometry at the Izaña High Mountain Observatory. *Atmos. Meas. Tech.* **2017**, *10*, 3007–3019. [CrossRef]
11. Wang, J.; Zhou, M.; Xu, X.; Roudini, S.; Sander, S.P.; Pongetti, T.J.; Miller, S.D.; Reid, J.S.; Hyer, E.; Spurr, R. Development of a Nighttime Shortwave Radiative Transfer Model for Remote Sensing of Nocturnal Aerosols and Fires from VIIRS. *Remote Sens. Environ.* **2020**, *241*, 111727. [CrossRef]
12. Perrone, M.R.; Lorusso, A.; Romano, S. Diurnal and Nocturnal Aerosol Properties by AERONET Sun-Sky-Lunar Photometer Measurements along Four Years. *Atmos. Res.* **2022**, *265*, 105889. [CrossRef]
13. Zhou, M.; Wang, J.; Chen, X.; Xu, X.; Colarco, P.R.; Miller, S.D.; Reid, J.S.; Kondragunta, S.; Giles, D.M.; Holben, B. Nighttime Smoke Aerosol Optical Depth over the U.S. Rural Areas: First Retrieval from VIIRS Moonlight Observations. *Remote Sens. Environ.* **2021**, *267*, 112717. [CrossRef]
14. Miller, S.D.; Combs, C.L.; Kidder, S.Q.; Lee, T.F. Assessing Moonlight Availability for Nighttime Environmental Applications by Low-Light Visible Polar-Orbiting Satellite Sensors. *J. Atmos. Ocean. Technol.* **2012**, *29*, 538–557. [CrossRef]
15. Kocifaj, M.; Bará, S. Diffuse Light around Cities: New Perspectives in Satellite Remote Sensing of Nighttime Aerosols. *Atmos. Res.* **2022**, *266*, 105969. [CrossRef]
16. Zhang, J.; Reid, J.S.; Miller, S.D.; Turk, F.J. Strategy for Studying Nocturnal Aerosol Optical Depth Using Artificial Lights. *Int. J. Remote Sens.* **2008**, *29*, 4599–4613. [CrossRef]
17. Johnson, R.S.; Zhang, J.; Hyer, E.J.; Miller, S.D.; Reid, J.S. Preliminary Investigations toward Nighttime Aerosol Optical Depth Retrievals from the VIIRS Day/Night Band. *Atmos. Meas. Tech.* **2013**, *6*, 1245–1255. [CrossRef]
18. McHardy, T.M.; Zhang, J.; Reid, J.S.; Miller, S.D.; Hyer, E.J.; Kuehn, R.E. An Improved Method for Retrieving Nighttime Aerosol Optical Thickness from the VIIRS Day/Night Band. *Atmos. Meas. Tech.* **2015**, *8*, 4773–4783. [CrossRef]
19. Zhang, J.; Jaker, S.L.; Reid, J.S.; Miller, S.D.; Solbrig, J.; Toth, T.D. Characterization and Application of Artificial Light Sources for Nighttime Aerosol Optical Depth Retrievals Using the Visible Infrared Imager Radiometer Suite Day/Night Band. *Atmos. Meas. Tech.* **2019**, *12*, 3209–3222. [CrossRef]
20. Wang, X.; Mu, X.; Yan, G. Quantitative Analysis of Aerosol Influence on Suomi-NPP VIIRS Nighttime Light in China. *IEEE J. Sel. Top. Appl. Earth Obs. Remote Sens.* **2020**, *13*, 3557–3568. [CrossRef]
21. Jiang, M.; Chen, L.; He, Y.; Hu, X.; Liu, M.; Zhang, P. Nighttime Aerosol Optical Depth Retrievals from VIIRS Day/Night Band Data. *Natl. Remote Sens. Bull.* **2022**, *26*, 493–504. [CrossRef]
22. Li, H.; Hu, S.; Ma, S.; Tan, Z.; Ai, W.; Yan, W. Retrieving Nighttime Aerosol Optical Depth Using Combined Measurements of Satellite Low Light Channels and Ground-Based Integrating Spheres. *Int. J. Remote Sens.* **2024**, *45*, 7902–7914. [CrossRef]
23. Meng, Y.; Zhou, J.; Wang, Z.; Tang, W.; Ma, J.; Zhang, T.; Long, Z. Retrieval of Nighttime Aerosol Optical Depth by Simultaneous Consideration of Artificial and Natural Light Sources. *Sci. Total Environ.* **2023**, *896*, 166354. [CrossRef]
24. Chen, X.; Zhang, W.; He, J.; Zhang, L.; Guo, H.; Li, J.; Gu, X. Mapping PM2.5 Concentration from the Top-of-Atmosphere Reflectance of Himawari-8 via an Ensemble Stacking Model. *Atmos. Environ.* **2024**, *330*, 120560. [CrossRef]
25. Li, T.; Li, B.; Han, Z.; Zhang, W.; Yang, X. Nighttime PM2.5 Concentration Estimation Based on NPP-VIIRS and Interpretable Machine Learning: The Case of Beijing–Tianjin–Hebei Region. *IEEE J. Sel. Top. Appl. Earth Obs. Remote Sens.* **2025**, *18*, 11047–11059. [CrossRef]
26. Jiang, M.; Sun, W.; Yang, G.; Zhang, D. Modelling Seasonal GWR of Daily PM2.5 with Proper Auxiliary Variables for the Yangtze River Delta. *Remote Sens.* **2017**, *9*, 346. [CrossRef]
27. Hersbach, H.; Bell, B.; Berrisford, P.; Hirahara, S.; Horányi, A.; Muñoz-Sabater, J.; Nicolas, J.; Peubey, C.; Radu, R.; Schepers, D.; et al. The ERA5 Global Reanalysis. *Q. J. R. Meteorol. Soc.* **2020**, *146*, 1999–2049. [CrossRef]
28. He, J.; Zhang, W.; Liu, S.; Zhang, L.; Liu, Q.; Gu, X.; Yu, T. Applicability Analysis of Three Atmospheric Radiative Transfer Models in Nighttime. *Atmosphere* **2024**, *15*, 126. [CrossRef]
29. Inness, A.; Ades, M.; Agustí-Panareda, A.; Barré, J.; Benedictow, A.; Blechschmidt, A.-M.; Dominguez, J.J.; Engelen, R.; Eskes, H.; Flemming, J.; et al. The CAMS Reanalysis of Atmospheric Composition. *Atmos. Chem. Phys.* **2019**, *19*, 3515–3556. [CrossRef]
30. Ma, Y.; Zhang, W.; Chen, X.; Zhang, L.; Liu, Q. High Spatial Resolution Nighttime PM2.5 Datasets in the Beijing–Tianjin–Hebei Region from 2015 to 2021 using VIIRS/DNB and Deep Learning Model. *Remote Sens.* **2023**, *15*, 4271. [CrossRef]
31. Farr, T.G.; Rosen, P.A.; Caro, E.; Crippen, R.; Duren, R.; Hensley, S.; Kobrick, M.; Paller, M.; Rodriguez, E.; Roth, L.; et al. The Shuttle Radar Topography Mission. *Rev. Geophys.* **2007**, *45*, RG000183. [CrossRef]
32. Chen, Y.; Jiao, S.; Gu, X.; Li, S. Decoding the Spatiotemporal Effects of Industrial Clusters on Carbon Emissions in a Chinese River Basin. *J. Clean. Prod.* **2025**, *516*, 145851. [CrossRef]

33. Zhang, H.; Zhan, Y.; Li, J.; Chao, C.-Y.; Liu, Q.; Wang, C.; Jia, S.; Ma, L.; Biswas, P. Using Kriging Incorporated with Wind Direction to Investigate Ground-Level PM2.5 Concentration. *Sci. Total Environ.* **2021**, *751*, 141813. [CrossRef]
34. Wang, Z.; Chen, P.; Wang, R.; An, Z.; Qiu, L. Estimation of PM2.5 Concentrations with High Spatiotemporal Resolution in Beijing Using the ERA5 Dataset and Machine Learning Models. *Adv. Space Res.* **2023**, *71*, 3150–3165. [CrossRef]

Disclaimer/Publisher's Note: The statements, opinions and data contained in all publications are solely those of the individual author(s) and contributor(s) and not of MDPI and/or the editor(s). MDPI and/or the editor(s) disclaim responsibility for any injury to people or property resulting from any ideas, methods, instructions or products referred to in the content.